International Communications in Heat and Mass Transfer 175 (2026) 111078

Contents lists available at ScienceDirect

International Communications in Heat and Mass Transfer

journal homepage: www.elsevier.com/locate/ichmt

Multi-component vaporisation: Tabulated distillation curve models for ideal atmospheric-pressure conditions

Maximilian Dammann [a,b,c,*], Marco Mancini [c], Thomas Kolb [a,b], Roman Weber [c]

[a] Karlsruhe Institute of Technology (KIT), Engler-Bunte-Institute, Fuel Technology (EBI ceb), Engler-Bunte-Ring 1, 76131 Karlsruhe, Germany
[b] Karlsruhe Institute of Technology (KIT), Institute for Technical Chemistry, Gasification Technology (ITC vgt), Hermann-von-Helmholtz-Platz 1, 76344 Eggenstein-Leopoldshafen, Germany
[c] Clausthal University of Technology, Institute for Energy Process Engineering and Fuel Technology (IEVB), Agricolastraße 4, 38678 Clausthal-Zellerfeld, Germany

ARTICLE INFO

Keywords:
Vaporisation
Evaporation
Droplet
Combustion
Entrained flow
Gasification

ABSTRACT

Multi-component vaporisation of liquid fuels in combustion processes is typically described using simplified approaches for computing time reasons. Existing approaches include surrogate, continuous thermodynamics, quasi-discrete component and distillation curve models. These approaches, however, strongly simplify composition and physical properties and hence the vaporisation behaviour when applied to technical fuels with numerous species from different chemical classes. Therefore, this study developed a new approach for an accurate and efficient mathematical description of single-droplet vaporisation of complex technical fuels. This approach utilises the link between distillation and vaporisation, assumes rapid internal mixing and isobaric conditions and employs tabulated distillation curve models. These models are based on tabulated equilibrium distillation and physical property curves and have thus a theoretical basis in contrast to previous distillation curve models. In this study, tabulated distillation curve models are presented for a pure liquid compound, a bi-component liquid and a liquid technical fuel assuming ideal atmospheric-pressure conditions. In addition, single-droplet vaporisation predictions based on these models are compared with predictions based on discrete component models. The comparisons show that tabulated distillation curve models can describe the vaporisation of multi-component liquids under ideal conditions with similar accuracy as discrete component models when using the same physical property models. The predictions also highlight an often overlooked aspect that the development of vaporisation models for technical fuels has to be assisted with the generation of appropriate physical property data. Furthermore, the single-droplet vaporisation simulations suggest that, for any multi-component liquid, tabulated distillation curve models require similar computing times as discrete component models with eight components.

1. Introduction

Vaporisation of single- and multi-component droplets has extensively been studied using experiments and simulations for decades due to the wide range of applications of liquid fuels in industrial combustion processes. Liquid fuels can consist of up to hundreds of species from different chemical classes (e. g. *n*-alkanes, iso-alkanes, cyclo-alkanes, alkenes, aromatics, alcohols, ethers and naphthalenes). Limited only by fuel variability, fuel volatility and peak assignment, the contents of these species can nowadays be determined using coupled gas chromatography–mass spectrometry (GC–MS) analyses. For example, previous studies have provided GC–MS data sets for diesel [1], gasoline [2], fossil jet fuels [3] and alternative jet fuels [4]. These data sets are an excellent basis for three-dimensional transient vaporisation simulations of multi-component droplets. Such detailed simulations, however, can be conducted only for selected operating conditions due to computing time reasons [5–10]. In addition, the uncertainties and inaccuracies associated with common physical property methods and databases have a major impact on the predictions. Therefore, numerical simulations of technical processes with multi-component vaporisation phenomena are typically conducted using simplified models. These models assume local thermal equilibria inside droplets as well as specific distributions of temperature and species concentrations in droplets and film layers. For example, rapid mixing or infinite thermal conductivity and diffusivity (ITC/ID) models neglect the internal heat and mass transfer and are therefore based on uniform distributions of droplet temperature and droplet species concentrations at each time step. Effective thermal conductivity and diffusivity

* Corresponding author.
E-mail address: maximilian.dammann@kit.edu (M. Dammann).

https://doi.org/10.1016/j.icheatmasstransfer.2026.111078

Available online 11 April 2026

Nomenclature

Latin symbols

A	area
B	Spalding number
C	coefficient
$\hat{C}$	specific heat capacity
d	diameter
D	correction factor
D	diffusion coefficient
f	factor
F	correction factor
g	Earth acceleration
h	heat transfer coefficient
$\hat{H}$	specific enthalpy
$\Delta_{\mathrm{vap}}\hat{H}$	specific enthalpy of vaporisation
k	constant
K	equilibrium coefficient
Le	Lewis number
m	mass
M	molar mass
Nu	Nusselt number
p	pressure
Pe	Peclet number
Pr	Prandtl number
r	volume fraction
Re	Reynolds number
Sc	Schmidt number
Sh	Sherwood number
t	time
T	temperature
u	velocity
w	mass fraction
$\boldsymbol{w}$	mass fraction vector
x	mole fraction
$\boldsymbol{x}$	mole fraction vector
x	position

Greek symbols

γ	activity coefficient
Δ	difference
ϵ	characteristic Lennard–Jones energy parameter
ε	vaporisation mass fraction
$\boldsymbol{\epsilon}$	vaporisation mass fraction vector
η	dynamic viscosity
λ	thermal conductivity
ρ	density
σ	characteristic Lennard–Jones length
τ	relaxation time
φ	auxiliary model parameter
φ	fugacity coefficient
ω	acentric factor

Subscripts and superscripts

B	Boltzmann
boil	boiling
c	critical
conv	convective
d	drag
d	for droplet diameter predictions
DC	based on the discrete component model
dist	distillation
eff	effective
evap	of the vaporising mixture
film	at film condition, film
gas	gas, of the gas phase
i	of species i, of quasi-component i
inert	of inert gas
liq	liquid, of the liquid phase, droplet, of the droplet
m	with respect to mass transfer
max	maximum
min	minimum
mod	modified
p	isobaric
phys	physical
s	at the surface, surface
sat	at the saturated state
T	for droplet temperature predictions
T	with respect to heat transfer
TDC	based on the tabulated distillation curve model
u	for droplet velocity predictions
vap	vapour, of the vapour phase
x	for droplet position predictions
0	based on Ranz–Marshall correlation
0	initial
β	recovered

Acronyms

AD	absolute deviation
ASTM	American Society for Testing Materials
AtJ	Alcohol-to-Jet
CFD	computational fluid dynamics
CT	continuous thermodynamics
DC	discrete component
ETC/ED	effective thermal conductivity and diffusivity
GC–MS	gas chromatography–mass spectrometry
ID	integral deviation
ITC/ID	infinite thermal conductivity and diffusivity
QDC	quasi-discrete component
RD	relative deviation
TDC	tabulated distillation curve
UNIFAC	Universal Quasichemical Functional Group Activity Coefficients

(ETC/ED) models, in turn, assume one-dimensional profiles of droplet temperature and droplet species concentrations, while correcting the thermal conductivity and the species diffusion coefficients using algebraic expressions derived from detailed simulations [11]. However, ETC/ED models already increase significantly the computing times for technical processes. Therefore, ITC/ID models are usually employed for CFD simulations of these processes [12–14].

Furthermore, simplified models are combined with discrete component, surrogate, continuous thermodynamics, hybrid, quasi-discrete component and distillation curves models. Discrete component (DC)

models account for all (identifiable) species of multi-component mixtures and can therefore be considered as reference models. Surrogate, continuous thermodynamics, hybrid, quasi-discrete component and distillation curves models, in turn, simplify the description of multi-component mixtures, while maintaining high levels of accuracy and efficiency for CFD simulations of technical processes. The advantages and disadvantages of these models are discussed in Sections 1.1, 1.2, 1.3, 1.4 and 1.5, before the objectives of this study are presented in Section 1.6.

1.1. Surrogate models

Surrogate models are discrete component models of surrogates, i. e. well-defined mixtures. The compositions of the surrogates are usually determined considering the characteristic experimental data of a technical fuel. These data can include the Research Octane Number (according to ASTM D2699-15a), the Motor Octane Number (according to ASTM D2700-16), the derived cetane number, the hydrogen/carbon ratio, the molar mass, the composition, the heating value, functional groups, ignition delay times, flame speeds, emissions, heating and vaporisation characteristics, distillation curves, and specific gravities [2,15–24]. Moreover, surrogates can be derived using advanced optimisation methods, such as the multiple target approach [17] or the minimalist functional group approach [23,24]. The definition of (new) surrogates thus requires detailed analyses of the chemical and physical properties of both possible surrogates and the technical fuel, while accepting that surrogates are strong simplifications of multi-component mixtures. However, surrogates allow reproducing experiments and developing simplified models of technical processes and have therefore been suggested for jet fuels [15,16,25], gasolines [2,17,18,26–28], diesel [19,20,26,27,29] and heavy fuels [30,31].

1.2. Continuous thermodynamics models

Continuous thermodynamics (CT) models (see Section S1) describe the vaporisation of multi-component mixtures using presumed probability density functions and two (mean and variance) transport equations for each chemical class. The presumed probability density functions have been developed using gamma or double gamma distributions of molar mass or boiling temperature [32–39]. Moreover, CT models have provided reasonable mathematical descriptions for the vaporisation of multi-component mixtures [32–37,40–44] and have been efficient for CFD simulations, including large eddy simulations [14,45] and direct numerical simulations [46,47]. However, CT models have three deficiencies. Firstly, the accuracy of the probability density functions is not sufficient to describe chemical classes with a few species of different carbon number. Secondly, the physical properties have to be provided as a function of the distribution quantity or the distribution mean [14,32,35,37,44]. Thirdly, representative vapour species have to be chosen for the gas species balance equations. For the combustion of Jet A-1, Eckel [14] recently selected *n*-dodecane, iso-octane, cyclo-hexane and toluene as representative species for the *n*-alkanes, iso-alkanes, cyclo-alkanes and mono-aromatics, respectively.

1.3. Hybrid models

Hybrid models are combinations of continuous thermodynamics models and surrogate models and have been used to describe the vaporisation of diesel–bio-oil mixtures, diesel–bio-diesel mixtures and gasoline–ethanol mixtures [22,48,49]. The continuous thermodynamics approach has been employed for diesel and gasoline, while the surrogate/discrete component approach has been used for bio-oil, bio-diesel and ethanol [22,48,49]. In comparison with continuous thermodynamics models and discrete component models, hybrid models have provided the best compromise between computational accuracy and efficiency [50]. However, these models retain the deficiencies of both surrogate models and continuous thermodynamics models.

1.4. Quasi-discrete component models

Quasi-discrete component (QDC) models (see Section S2) describe the vaporisation of multi-component mixtures using quasi-components, i. e. chemical class-specific model components with well-defined carbon numbers. These numbers were determined previously using continuous or discrete chemical class-specific composition distributions [51,52]. QDC models allow to significantly reduce the number of components for vaporisation predictions if numerous species can be assigned to a few chemical classes. However, QDC models have three deficiencies. Firstly, 15–20 quasi-components are (still) required for accurate approximations of liquid technical fuels, such as diesel and gasoline [52,53]. Secondly, approximations are not accurate for technical fuels with components that belong to various chemical classes. Thirdly, for each chemical class, the physical properties have to be approximated as a function of the carbon number [51–54].

1.5. Distillation curve models

Distillation curve models (see Section S3) have been derived to describe the multi-component vaporisation of jet fuels under both atmospheric- and high-pressure conditions based on single-component rapid-mixing models [55–59]. The distillation curve models account for the progress of vaporisation and the impact of diffusion. The progress of vaporisation is identical to the recovered mass fraction used in distillation experiments or simulations. The impact of diffusion, in turn, has been incorporated through a distillation Peclet number [55,60], a fuel-specific intermittency function [55,56], and fuel-specific expressions for vapour pressure, molar mass of vapour, and molar enthalpy of vaporisation at both *zero diffusion resistance* (corresponding to the rapid-mixing model) and *infinite diffusion resistance* (corresponding to the thin-skin model) [55]. The fuel-specific intermittency functions were determined using one-dimensional two-component vaporisation predictions and subsequent regressions [55,56]. The (empirical) expressions at *zero diffusion resistance* were derived for gasolines, diesel and jet fuels [61–63] using ASTM D86 distillation curves (see Section 2.1) and additional empirical correlations. Furthermore, additional correlations were used to describe the physical properties of liquid and vapour. Chin [55] determined the physical properties of both phases as a function of the respective acentric factor and the respective molar mass. Prommersberger et al. [56,57] and Burger et al. [59,64], in turn, applied (i) correlations based on the critical temperatures and pressures of *n*-alkanes for calculating the acentric factor and (ii) further corresponding-state model equations, such as the Racket equation [65] for the density of the liquid phase.

The distillation curve models have maintained nearly the simplicity and efficiency of rapid-mixing models and provided results that were in good agreement with experimental data and simplified numerical predictions [55–59]. The models are thus very promising despite their complex empirical nature. However, to the best knowledge of the authors, the predictions based on distillation curve models have not yet been compared with predictions that were obtained using discrete components. Thus, the accuracy of distillation curve models has not been fully examined yet.

1.6. Objectives

Surrogate, continuous thermodynamics, hybrid, quasi-discrete component and distillation curve models are reasonable compromises between accuracy and efficiency. However, developing these models requires detailed experimental or numerical analyses as well as fuel-specific assumptions or correlations. This applies in particular to distillation curve models, which are based on numerous empirical approaches. Therefore, these models have been adapted to a few multi-component mixtures only and have not yet been examined further. Only two studies [66,67] focussed recently on both distillation and

vaporisation behaviour of multi-component mixtures. Govindaraju and Ihme [66] compared fractional and flash distillation curves of jet fuels and gasolines with (experimental) advanced distillation curves [68, 69] and analysed the distillation and multi-component vaporisation behaviour of gasoline blends. Burke et al. [67] conducted distillation experiments and simulations for various ethanol–FACE B gasoline blends and investigated the effects of blending on vaporisation and distillation behaviour. Thus, both Govindaraju and Ihme [66] and Burke et al. [67] considered distillation and vaporisation as two different approaches. However, distillation is strongly linked to vaporisation. This link was used in this study for generating models that overcome most of the deficiencies of surrogate, continuous thermodynamics, hybrid, quasi-discrete component and distillation curve models, assuming isobaric conditions and uniform distributions of droplet temperature and droplet species concentrations. The new models are based on tabulated thermodynamic state and physical property curves and are briefly referred to as tabulated distillation curve (TDC) models.

The model fundamentals of experimental and numerical distillation curves are summarised in Section 2. The methods for generating tabulated distillation curves are presented in Section 3. The models used to conduct single-droplet vaporisation simulations based on TDC models or DC models are described in Section 4. The single-droplet vaporisation predictions are compared and discussed in Section 5. The conclusions are given in Section 6.

2. Distillation curves

Distillation curves are vapour–liquid equilibrium curves providing the boiling temperature T_{boil} as a function of the recovered volume fraction r_β (or the recovered mole fraction x_β or the recovered mass fraction w_β). The curves can be determined using both experimental and numerical methods. The experimental methods are presented in Section 2.1, while the numerical methods are described in Section 2.2.

2.1. Experimental distillation curves

Experimental distillation curves are measured using batch distillation apparatus. The most common apparatus is based on ASTM D86 [70] and is used to measure (i) the initial and final boiling temperatures and (ii) the boiling temperatures at recovered volume fractions of 10%, 20%, 30%, 40%, 50%, 60%, 70%, 80% and 90%. Following previous reviews [71,72], experimental distillation curves based on ASTM D86 [73] are subject to certain restrictions if it comes to comparisons with theoretical distillation curves. This is due to the methodical measurement uncertainties for pressure, temperature and recovered volume fraction. Several recommendations and modifications have been proposed [71,72,74] to get results that are both more reliable and more comparable with theoretical results. For example, time-resolved measurements can be used to improve the measured temperatures and recovered volume fractions [72]. In addition, minor deviations from standard pressure of 1 atm can be corrected using the Sydney–Young equation [72]. By introducing new definitions for the initial and the final boiling temperatures and by shifting the liquid temperatures at recovered volume fractions between 5% and 95%, Ferris and Rothamer [72] recently presented experimental distillation curves that were in excellent agreement with theoretical ones. However, most of the distillation data has been derived based on ASTM D86 [73]. Therefore, distillation data that was used as basis of comparison in this study is based on experiments following ASTM D86 [4].

2.2. Numerical distillation curves

Numerical distillation curves can be determined without measurement uncertainties and with high numerical accuracy. However, the calculation of these curves requires accurate composition and physical property data. While such data are typically given for model mixtures, larger challenges are faced for technical fuels. Firstly, GC–MS analyses do not always allow to identify all species and to provide complete fuel compositions. Secondly, accurate expressions for vapour pressures, densities, activity coefficients and fugacity coefficients are not available for all fuel compounds and need to be estimated using group contribution and corresponding-states methods. Therefore, numerical distillation curves are not necessarily superior to experimental distillation curves and are usually given as equilibrium distillation, flash distillation and fractional distillation curves. These three different curves are introduced in Sections 2.2.1, 2.2.2 and 2.2.3 and are compared in Section 2.2.4.

2.2.1. Flash distillation curves

Flash distillation curves are based on equilibrium batch balances, which are defined for a pressure p and for temperatures between an initial temperature T_0 and a maximum temperature T_{max}. Firstly, the recovered mole fraction x_β is calculated by

$$\sum_i \frac{x_{i,\mathrm{liq},0}}{\frac{1}{K_i - 1} + x_\beta} = 0\,, \tag{1}$$

where $x_{i,\mathrm{liq},0}$ is the initial mole fraction of species i in the liquid phase and K_i is the equilibrium coefficient of species i. Secondly, the compositions of the vapour phase (in mole fractions $\boldsymbol{x}_{\mathrm{vap}}$) and the liquid phase (in mole fractions $\boldsymbol{x}_{\mathrm{liq}}$) are determined using species balances. These two steps are repeated until the distillation batch is completely vaporised, i. e. until the iteration based on Eq. (1) returns one for the recovered mole fraction x_β. The equilibrium coefficient K of species i is defined by

$$K_i = \begin{cases} \frac{p_{i,\mathrm{vap}}(T)}{p}\,, & \text{if ideal liquid and ideal vapour} \\ \gamma_i \frac{p_{i,\mathrm{vap}}(T)}{p}\,, & \text{if real liquid (based on activity coefficients) and ideal vapour} \\ \gamma_i \frac{\varphi_{i,\mathrm{sat}}\, p_{i,\mathrm{vap}}(T)}{\varphi_{i,\mathrm{vap}}\, p}\,, & \text{if real liquid (based on both activity and fugacity coefficients) and real vapour} \\ \frac{\varphi_{i,\mathrm{liq}}}{\varphi_{i,\mathrm{vap}}}\,, & \text{if real liquid (based on fugacity coefficients) and real vapour} \end{cases}, \tag{2}$$

where γ_i is the activity coefficient of species i (based on the composition of the liquid phase), $\varphi_{i,\mathrm{liq}}$ is the fugacity coefficient of species i in the liquid phase (based on the composition of the liquid phase), $\varphi_{i,\mathrm{vap}}$ is the fugacity coefficient of species i in the vapour phase (based on the composition of the liquid phase) and $\varphi_{i,\mathrm{sat}}$ is the fugacity coefficient of species i at the saturated state.

2.2.2. Fractional distillation curves

Fractional distillation curves are determined using the order of the species according to their boiling temperatures at a pressure p. Firstly, it is assumed that the species with the lowest boiling temperature T_{boil} vaporises from the liquid distillation batch. Secondly, the compositions of the vapour phase in mole fractions $\boldsymbol{x}_{\mathrm{vap}}$ and the liquid phase in mole fractions $\boldsymbol{x}_{\mathrm{liq}}$ as well as the recovered mole fraction x_β are updated in accordance with the species balances. These two steps are repeated until the distillation batch is completely vaporised.

2.2.3. Equilibrium distillation curves

Equilibrium distillation curves are determined assuming phase equilibria between liquid and vapour. Firstly, the boiling temperature T_{boil} is calculated by

$$p - \sum_i x_{i,\mathrm{liq}}\, K_i\left(T_{\mathrm{boil}}\right)\, p = 0\,, \tag{3}$$

where $x_{i,\mathrm{liq}}$ is the mole fraction of species i in the liquid phase and K_i is the equilibrium coefficient of species i (see Eq. (2)). Note that

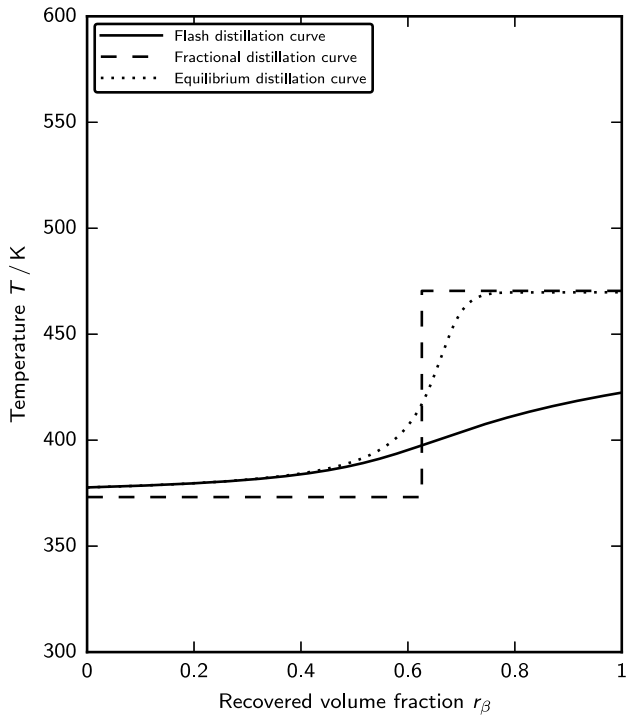

Fig. 1. Numerical flash, fractional and equilibrium distillation curves for the ethylene glycol–water mixture.

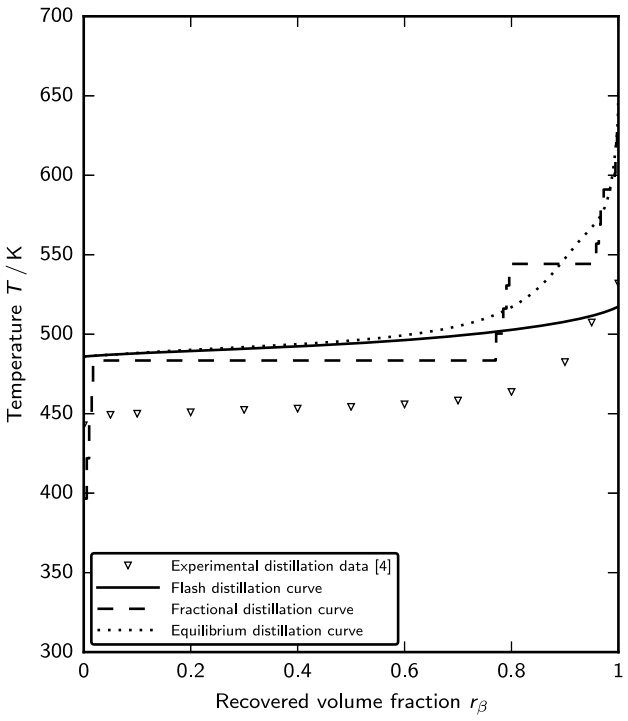

Fig. 2. Numerical flash, fractional and equilibrium distillation and experimental distillation curves for AtJ.

the pressure p in the second term of the left-hand side of Eq. (3) vanishes when substituting the equilibrium coefficient and assuming ideal gas behaviour for the vapour phase. Secondly, the composition of the vapour phase in mole fractions $\boldsymbol{x}_{\text{vap}}$ is determined assuming equilibrium, while the composition of the liquid phase in mole fractions $\boldsymbol{x}_{\text{liq}}$ is updated in accordance with the change of the composition of the vapour phase. These two steps are repeated until the distillation batch is completely vaporised.

2.2.4. Comparisons

Flash distillation, fractional distillation and equilibrium distillation curves were calculated, assuming ideal liquid and vapour phases, (i) for a bi-component mixture consisting of 50% ethylene glycol and 50% water (in mass fractions) using the physical property methods and databases of Aspen Properties [75] and (ii) for the technical jet fuel AtJ [4] using the group contribution methods of Constantionou and Gani [76] and the Lee–Kessler equation [77]. The numerical distillation curves are shown for the bi-component mixture in Fig. 1 and for the technical jet fuel in Fig. 2. In addition, ASTM D86 distillation data [4] is shown in Fig. 2. Firstly, the flash distillation curves approximate the equilibrium distillation curves at the initial stages, while the fractional distillation curves approximate the equilibrium distillation curves at the final stages. This is in agreement with previous observations [66,72] and in line with the expectation that equilibrium distillation curves should provide the best possible approximation of the distillation behaviour. Secondly, the experimental distillation data and the numerical equilibrium distillation curve have similar patterns for AtJ but differ clearly from each other. This is because the accuracy of the physical property models employed is not sufficient for the compounds of AtJ. However, these models were applied in the further course of this study (see Section 3.2) since (i) it was beyond the objective of this study to determine the most appropriate physical property models and (ii) the method for generating TDC models is valid for any set of physical property models, methods and databases.

3. Tabulated distillation curves

Tabulated distillation curves comprise adapted equilibrium distillation curves and physical property curves. These curves are described in Sections 3.1 and 3.2 and are obtained using (i) relevant thermodynamic conditions of droplet vaporisation, (ii) selected tabulation variables and (iii) appropriate grids for the tabulation variables. Further details are given in Sections 3.3, 3.4 and 3.5. The tabulated curves are presented for three mixtures in Section 3.6, while the access to the tables using linear interpolation is described in Section 3.7.

3.1. Adapted equilibrium distillation curves

Adapted equilibrium distillation curves represent possible thermodynamic equilibrium states during the vaporisation of droplets, assuming isobaric conditions and uniform distributions of droplet temperature and droplet species concentrations. The curves can be generated following the approach for standard equilibrium distillation curves (see Section 2.2.3). Adapted equilibrium distillation curves, however, assume a gas phase consisting of vapour and inert gas, in contrast to standard equilibrium distillation curves, which are calculated for a system with a liquid phase and a vapour phase at a constant pressure p (see Section 2.2.3). Therefore, the total pressure p in the first term of Eq. (3) is replaced by a partial pressure $x_{\text{vap}}\, p$, where $x_{\text{vap}} = 1 - x_{\text{inert}}$ is the mole fraction of vapour and x_{inert} is the mole fraction of inert gas. The equilibrium distillation temperature is calculated by

$$p\,\left(1 - x_{\text{inert}}\right) - \sum_i x_{i,\text{liq}}\, K_i\, p = 0\,. \tag{4}$$

All further calculation steps do not change. In particular, the composition of the vapour phase in mole fractions $\boldsymbol{x}_{\text{vap}}$ is still calculated using the total pressure p.

3.2. Physical property curves

Physical property curves describe the physical properties at the thermodynamic equilibrium states and were calculated using two sets of physical property models, methods and databases:

- Set A has been compiled for model mixtures and is based on the ideal equation of state, the physical property methods and databases of Aspen Properties [75], the Chapman–Enskog equation for the effective diffusion coefficients of the gas species [78], and the corresponding-states equation of Bondi [79] for the specific heat capacities of some liquid species, which are not accounted for by the methods and databases of Aspen Properties [75].
- Set B has been composed for technical fuels following the study of Govindaraju and Ihme [66], as even the physical property methods and databases of Aspen Properties [75] do not include all compounds that prevail in technical fuels. Set B is based on the ideal equation of state, the group contribution methods of Constantionou and Gani [76], the Lee–Kessler equation [77], the Chapman–Enskog equations for the dynamic viscosities, thermal conductivities and effective diffusion coefficients of the gas species and the corresponding-states equation of Bondi [79] for the specific heat capacities of the liquid species. The group contribution methods of Constantionou and Gani [76] were preferred to more recent methods, such as the methods of Nannoolal et al. [80–82] and Moller et al. [83]. This was because the methods of Constantionou and Gani [76] are based on similar group assignments as the UNIFAC method [84–86], which, in turn, may be used for the development of tabulated distillation curve models for non-ideal conditions in subsequent studies. However, future studies may also incorporate more recent group contribution methods.

The physical property models, methods and databases of both sets are summarised in Table 1.

3.3. Relevant thermodynamic conditions

Droplets in combustion processes are typically generated through atomisation of continuous liquids. The droplets enter hot environments, such as flame zones, and are heated up under high heating rates, while the vaporised species in the film boundary layer may also ignite in oxygen-rich atmospheres. The typical initial droplet temperatures are approximately 300 K, while the final ones seldom reach 1000 K in simulations. The simulated gas temperatures, in turn, depend on the chemistry models and can be up to 3500 K when the chemical reactions are described using global mechanisms. The film temperatures, which are typically based on the 1/3 rule and are calculated for several physical properties in single-droplet vaporisation simulations (see Section 4), are thus between 300 K and 2000 K.

3.4. Tabulation variables

Adapted equilibrium distillation curves are primarily determined as a function of the recovered mass fraction w_β and the mole fraction of vapour x_{vap}. The recovered mass fraction w_β is used to describe the distillation progress (see Section 2), while the mole fraction of vapour x_{vap} is applied to adapt the standard equilibrium distillation curve (see Section 3.1). Therefore, two-dimensional tables are generated using the recovered mass fraction w_β and the mole fraction of vapour x_{vap} as tabulation variables. Furthermore, several physical properties in single-droplet vaporisation models are evaluated at various film temperatures. Therefore, (additional) three-dimensional tables are created using the recovered mass fraction w_β, the mole fraction of vapour x_{vap} and the temperature T as tabulation variables.

The two-dimensional tables are generated for the distillation temperature T, the liquid species mass fractions, the vapour species mass fractions as well as the physical properties of the liquid phase, the vapour phase and the vaporising mixture. The physical properties include the molar mass M, the characteristic Lennard–Jones length σ, the characteristic Lennard–Jones energy parameter related to the Boltzmann constant ϵ/k_{B}, the acentric factor ω, the critical temperature T_{c}, the critical pressure p_{c}, the density ρ, the dynamic viscosity η, the thermal conductivity λ, the specific heat capacity $\hat{C}_p$, the specific physical enthalpy $\hat{H}_{\mathrm{phys}}$ and the specific enthalpy of vaporisation $\Delta_{\mathrm{vap}}\hat{H}$. It should be stressed that the physical properties of the vaporising mixture at a specific equilibrium distillation state are calculated using the composition of the mixture that is vaporising at this state, whereas the physical properties of both the liquid phase and the vapour phase are determined using the respective phase compositions present at this state.

The three-dimensional tables are determined for the density ρ, the dynamic viscosity η, the thermal conductivity λ, the specific heat capacity $\hat{C}_p$ and the specific physical enthalpy $\hat{H}_{\mathrm{phys}}$ of the vaporising mixture. These three-dimensional tables are realised through several two-dimensional tables, where each two-dimensional table provides the physical property as a function of the recovered mass fraction w_β and the temperature T for a specific mole fraction of vapour x_{vap}.

3.5. Tabulations grids

The tabulation grids for the recovered mass fraction w_β, the mole fraction of vapour x_{vap} and the temperature T were developed by comparing single-droplet vaporisation predictions based on TDC models with results based on DC models. The (baseline) grids are defined using the methods described below:

- The grid for the recovered mass fraction w_β is defined using 1001 grid points and an advanced non-equidistant spacing between zero and one. Firstly, the standard equilibrium distillation curve is calculated as a function of the recovered mass fraction w_β, where very small calculation steps provide several thousand points. Secondly, the absolute derivative of the standard equilibrium distillation curve is determined using the forward difference scheme in combination with a parabolic extrapolation at the last grid point. Thirdly, a cumulative distribution function is calculated for the absolute derivative data of the standard equilibrium distillation curve. Finally, inverse interpolation of the cumulative distribution function on an equidistant grid provides a gradient based grid, which significantly reduced the numerical errors of single-droplet vaporisation predictions based on TDC models.
- The grid for the mole fraction of vapour x_{vap} is determined using 41 grid points and a linear spacing between a minimum vaporisation temperature (that corresponds to a minimum mole fraction of vapour $x_{\mathrm{vap,min}}$) and a maximum vaporisation temperature (that corresponds to a maximum mole fraction of vapour $x_{\mathrm{vap,max}}$). The maximum possible mole fraction of vapour $x_{\mathrm{vap,max}}$ is given by one in accordance with the standard equilibrium distillation curve, while the minimum mole fraction of vapour $x_{\mathrm{vap,min}} > 0$ particularly depends on the operating pressure p and the initial vapour pressure p_{vap} at the droplet surface. The latter can be calculated using the initial droplet temperature $T_{\mathrm{liq},0}$ and the initial droplet composition in mole fractions $\boldsymbol{x}_{\mathrm{liq},0}$. Therefore, the criterion

$$x_{\mathrm{vap,min}} < \frac{p_{\mathrm{vap}}\big|_{T_{\mathrm{liq},0},\boldsymbol{x}_{\mathrm{liq},0}}}{p} \tag{5}$$

was applied to obtain an initial guess for the minimum mole fraction of vapour $x_{\mathrm{vap,min}}$. Repetitive tabulations and vaporisation simulations were subsequently used to optimise this value in order to ensure appropriate tabulations and accurate single-droplet vaporisation predictions.

Table 1
Physical property models, methods and databases of physical property sets A and B.

Physical property	Models, methods and databases	
	Set A	Set B
Molar mass of a species	Database of Aspen Properties [75]	Database of NASA [87]
Characteristic Lennard–Jones length of a species	Tee correlation [88]	Tee correlation [88]
Characteristic Lennard–Jones energy parameter of a species	Tee correlation [88]	Tee correlation [88]
Acentric factor of a species	Database of Aspen Properties [75]	Method of Constantionou and Gani [76]
Fugacity coefficient of a species	Ideal equation of state	Ideal equation of state
Activity coefficient of a species	Raoult equation	Raoult equation
Critical temperature of a species	Database of Aspen Properties [75]	Method of Constantionou and Gani [76]
Critical pressure of a species	Database of Aspen Properties [75]	Method of Constantionou and Gani [76]
Critical volume of a species	Database of Aspen Properties [75]	Method of Constantionou and Gani [76]
Density of a gas species	Ideal equation of state	Ideal equation of state
Dynamic viscosity of a gas species	Methods and databases of Aspen Properties [75]	Chapman–Enskog equation [78]
Thermal conductivity of a gas species	Methods and databases of Aspen Properties [75]	Chapman–Enskog equation [78]
Effective diffusion coefficient of a gas species	Chapman–Enskog equation [78]	Chapman–Enskog equation [78]
Specific heat capacity of a gas species	Methods and databases of Aspen Properties [75]	Method of Constantionou and Gani [76]
Density of a liquid species	Methods and databases of Aspen Properties [75]	Method of Constantionou and Gani [76] and method of Racket [78]
Dynamic viscosity of a liquid species	Methods and databases of Aspen Properties [75]	Constant
Effective diffusion coefficient of a liquid species	Wilke–Chang–Geankoplis equation [78,89]	Constant
Specific heat capacity of a liquid species	Methods and databases of Aspen Properties [75] and method of Bondi [79]	Method of Constantionou and Gani [76] and method of Bondi [79]
Characteristic Lennard–Jones length of a mixture	van der Waals mixing rule	van der Waals mixing rule
Characteristic Lennard–Jones energy parameter of a mixture	van der Waals mixing rule	van der Waals mixing rule
Critical temperature of a mixture	Mole-weighted mixing rule	Mole-weighted mixing rule
Critical pressure of a mixture	Mole-weighted mixing rule	Mole-weighted mixing rule
Critical volume of a mixture	Mole-weighted mixing rule	Mole-weighted mixing rule
Acentric factor of a mixture	Mole-weighted mixing rule	Mole-weighted mixing rule
Dynamic viscosity of a gas mixture	Wilke mixing rule [90]	Wilke mixing rule [90]
Thermal conductivity of a gas mixture	Wilke mixing rule [78,90]	Wilke mixing rule [78,90]
Specific heat capacity of a gas mixture	Mass-weighted mixing rule	Mass-weighted mixing rule
Dynamic viscosity of a liquid mixture	Grunberg–Nissan mixing rule [78,91]	Grunberg–Nissan mixing rule [78,91]
Thermal conductivity of a liquid mixture	Vredeveld mixing rule [78]	Vredeveld mixing rule [78]
Specific heat capacity of a liquid mixture	Mass-weighted mixing rule	Mass-weighted mixing rule

Table 2
Numbers of grid points for the recovered mass fraction w_β, the mole fraction of vapour x_{vap} and the temperature T.

Tabulation	Number of grid points		
	w_β	x_{vap}	T
Baseline	1001	41	36
Coarse	1001	21	36
Fine	10 001	81	71

- The grid for the temperature T was defined using 36 grid points and a logarithmic spacing between 300 K and 2000 K.

In addition to the baseline tabulation grids, both coarse and fine tabulation grids have been defined using different numbers of grid points for the mole fraction of vapour x_{vap}, the recovered mass fraction w_β and the temperature T to investigate the impact of the grid spacings. These numbers are given in Table 2.

3.6. Graphs

The distillation calculations and tabulations have been carried out for three liquids: (i) nonane, (ii) a bi-component mixture (50% ethylene glycol and 50% water, in mass fractions) and (iii) a technical fuel (AtJ [4]).

Adapted equilibrium distillation curves are shown for the three mixtures in Figs. S4 (left), 3 (left) and 4 (left). The distillation temperatures are constant for nonane, while they strongly change for the multi-component mixtures. Therefore, lower temperatures around 300 K are not tabulated at higher recovered mass fractions w_β for multi-component mixtures. This is usually not required as such conditions are not to be expected for combustion processes. However, if such conditions are likely, different settings and vapour–liquid equilibrium models need to be incorporated for calculating adapted equilibrium distillation curves.

Examples of the physical property curves are shown in Figs. 5 and 6 as well as Figs. S7–S12. Figs. 5 (left) and 6 (left) show the specific enthalpy of vaporisation of the vaporising mixtures $\Delta_{\text{vap}}\hat{H}$ during distillation. Due to the steep gradients, accurate adapted equilibrium distillation calculations and appropriate tabulation grids are required for the recovered mass fraction w_β (see Section 3.5). Moreover, Figs. 5 (right) and 6 (right) depict the specific heat capacity of the vaporising mixture $\hat{C}_{p,\text{evap}}$ during distillation. Note that (i) the temperature T is used for the colour bars instead of the mole fraction of vapour x_{vap} and (ii) various curves are plotted using the same colour to demonstrate the three-dimensional tabulation, where each curve corresponds to a specific mole fraction of vapour x_{vap}.

Furthermore, Figs. 3 (right) and 4 (right) show the vapour pressure p_{vap} during distillation. The vapour pressures p_{vap} were calculated using the distillation temperatures and the compositions of the liquid phase in mole fractions $\boldsymbol{x}_{\text{liq}}$. The curves are almost constant and in agreement with the specified vapour pressures $(1 - x_{\text{inert}})\,p$. This demonstrates that the adapted equilibrium distillation calculations provided data with small numerical errors. However, if too large calculation steps were used for the adapted equilibrium distillation calculations, the absolute error between the calculated vapour pressure p_{vap} and the specified vapour pressure $(1 - x_{\text{inert}})\,p$ would increase with increasing recovered mass fraction w_β. Moreover, the accuracy of single-droplet vaporisation predictions based on TDC models typically decreases with increasing errors in vapour pressure p_{vap}. Therefore, Figs. 3 (right) and 4 (right) should be used to check a-priori the accuracy of TDC models.

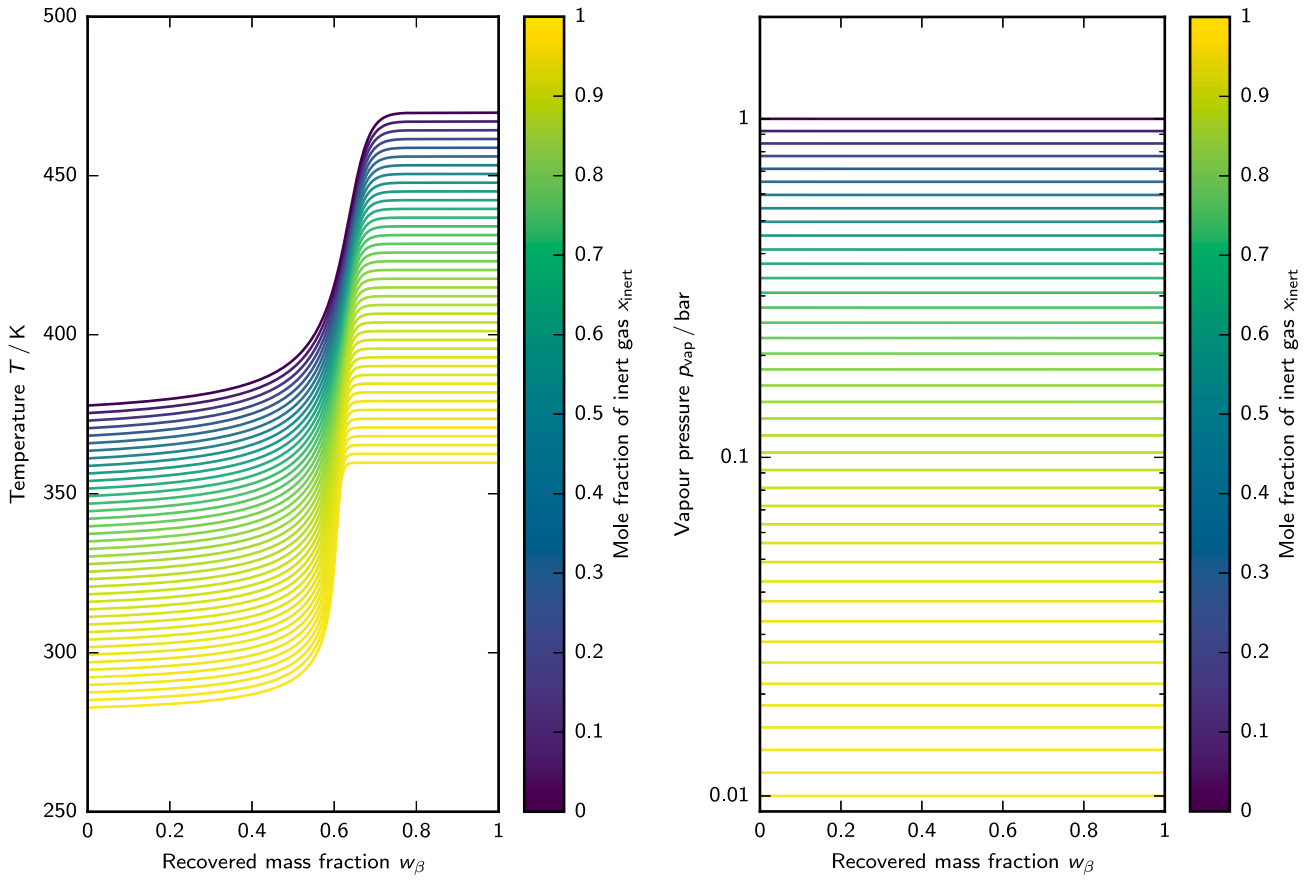

Fig. 3. Tabulated distillation curves (left) and tabulated curves of the vapour pressure p_{vap} (right) for the ethylene glycol–water mixture.

3.7. Access to the tables

The thermodynamic state and physical property tables are accessed using linear interpolation (for example, during single-droplet vaporisation simulations). First, after reading the tables into memory, the grids, used for the mole fraction of vapour x_{vap} and the recovered mass fraction w_β, are extracted from the tables. Then, the mole fraction of vapour x_{vap} and the indices of the nearest tabulated mole fractions of vapour are determined for a given droplet temperature T_{liq} and a given recovered mass fraction w_β using the tabulated distillation temperatures and inverse two-dimensional linear interpolation. Bounding based on constant values is applied if the queried droplet temperature T_{liq} or the queried recovered mass fraction w_β or the resulting mole fraction of vapour x_{vap} is outside the tabulation.

The mole fraction of vapour x_{vap} (based on the droplet temperature T_{liq}) and the recovered mass fraction w_β can be used to determine a physical property at the droplet temperature T_{liq}, for example, the specific enthalpy of vaporisation of the vaporising mixture $\Delta_{\text{vap}}\hat{H}$. The physical property value is calculated using two-dimensional linear interpolation, in combination with bounding based on constant values.

The mole fraction of vapour x_{vap} (based on the droplet temperature T_{liq}) and the recovered mass fraction w_β can also be employed to determine a physical property at a film temperature T_{film}. Firstly, the indices of the nearest tabulated mole fractions of vapour are determined. Secondly, these indices are used to identify the corresponding two-dimensional tables within the three-dimensional tabulation. Thirdly, the physical property value is calculated using three-dimensional linear interpolation in combination with bounding based on constant values.

4. Single-droplet vaporisation simulations

The single-droplet vaporisation simulations were carried out using a droplet motion model and a multi-component droplet vaporisation model, which was combined with either a tabulated distillation curve model or a discrete component model. The tabulated distillation curve model is based on the thermodynamic state and physical property tables, while the discrete component model accounts for all mixture compounds and relies on the physical property models that were used for generating the thermodynamic state and physical property tables (see Table 1). The model equations were implemented in an in-house software in Python and were solved using common numerical methods [92] and constant time steps.

4.1. Single-droplet motion model

The single-droplet motion model assumes an one-dimensional droplet flow in parallel to the gas flow. The droplet position x_{liq} is described by

$$\frac{\mathrm{d}x_{\text{liq}}}{\mathrm{d}t} = u_{\text{liq}}\,, \tag{6}$$

$$x_{\text{liq}}\Big|_{t=0} = x_{\text{liq},0}\,, \tag{7}$$

where t is the time, u_{liq} is the droplet velocity and $x_{\text{liq},0}$ is the initial droplet position. The droplet velocity u_{liq} is determined by

$$\frac{\mathrm{d}u_{\text{liq}}}{\mathrm{d}t} = \frac{1}{\tau_{\text{liq}}}\left(u_{\text{gas}} - u_{\text{liq}}\right) + \left(\rho_{\text{liq}} - \rho_{\text{gas}}\right)\frac{\pi}{6}\,d_{\text{liq}}^3\,g\,, \tag{8}$$

$$u_{\text{liq}}\Big|_{t=0} = u_{\text{liq},0}\,, \tag{9}$$

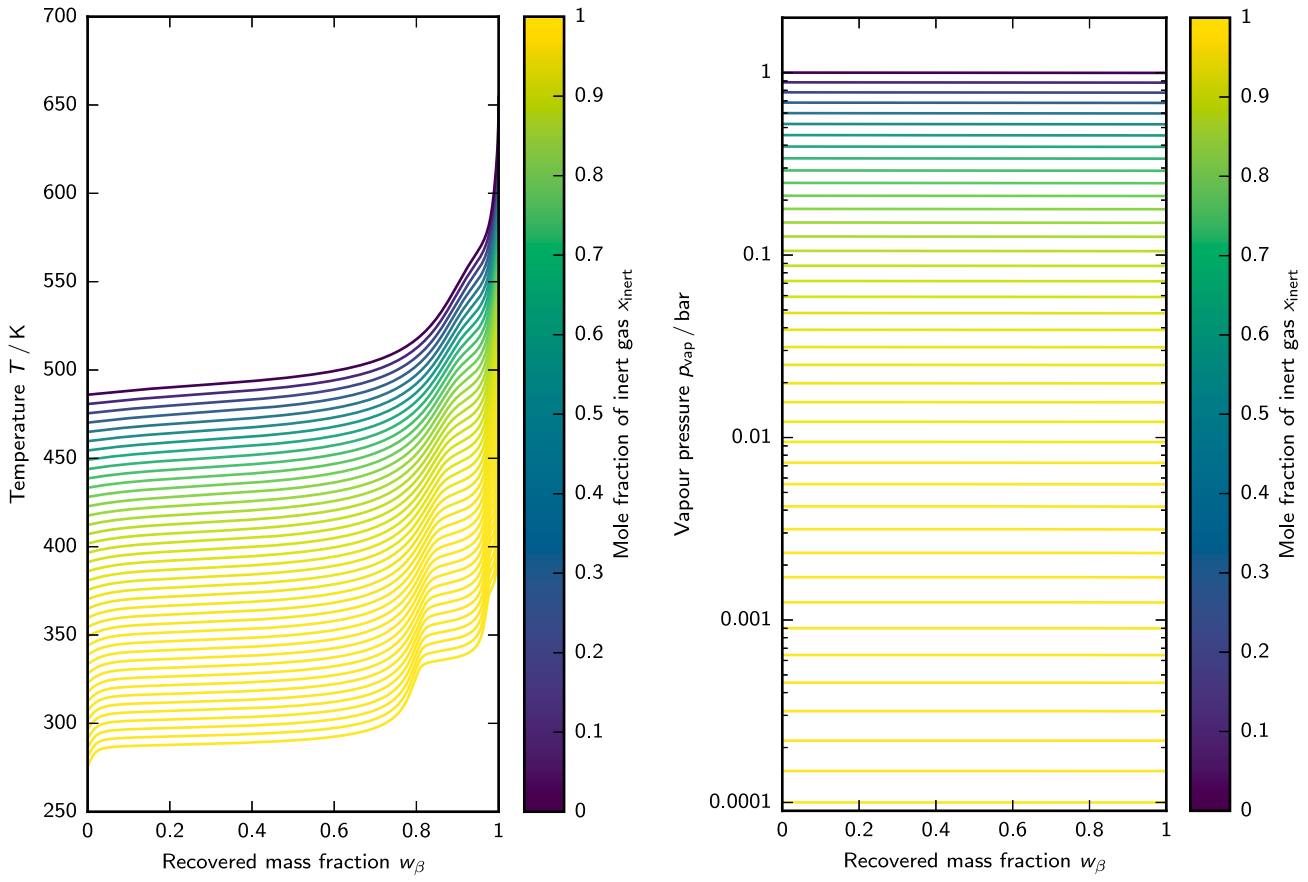

Fig. 4. Tabulated distillation curves (left) and tabulated curves of the vapour pressure p_{vap} (right) for AtJ.

where

$$\tau_{\text{liq}} = \frac{\rho_{\text{liq}}\, d_{\text{liq}}^2}{18\,\eta_{\text{gas}}}\,\frac{24}{C_{\text{d}}\, Re_{\text{liq}}}\,, \tag{10}$$

is the droplet relaxation time, u_{gas} is the gas velocity, ρ_{liq} is the droplet density, ρ_{gas} is the gas density, d_{liq} is the droplet diameter, g is the earth acceleration, $u_{\text{liq},0}$ is the initial droplet velocity, η_{gas} is the dynamic gas viscosity, C_{d} is the drag coefficient and $Re_{\text{liq}} = \rho_{\text{liq}}\, d_{\text{liq}}\, \left(u_{\text{liq}} - u_{\text{gas}}\right)/\eta_{\text{gas}}$ is the droplet Reynolds number. The drag coefficient C_{d} is calculated using the Morsi–Alexander equation [93].

4.2. Single-droplet vaporisation model

The single-droplet multi-component vaporisation model is based on the model of Abramzon and Sirignano [11], extended to multi-component mixtures but without adaptions or improvements following recent findings [10,94,95]. The model assumes a spherical droplet with uniform droplet temperature and droplet species concentrations at all time steps and describes the film boundary layer using a film temperature T_{film} and a gas film composition in mass fractions $\boldsymbol{w}_{\text{gas,film}}$. The film temperature T_{film} is given by [11]

$$T_{\text{film}} = T_{\text{liq,s}} + f_{\text{film}}\left(T_{\text{gas}} - T_{\text{liq,s}}\right)\,, \tag{11}$$

while the gas film composition in mass fractions $\boldsymbol{w}_{\text{gas,film}} = \left(w_{i,\text{gas,film}}\right)$ is determined by [11]

$$w_{i,\text{gas,film}} = w_{i,\text{gas,s}} + f_{\text{film}}\left(w_{i,\text{gas}} - w_{i,\text{gas,s}}\right)\,, \tag{12}$$

where $T_{\text{liq,s}}$ is the droplet surface temperature and is equal to the droplet temperature T_{liq} in the case of a uniform temperature distribution, f_{film} is the film factor, and $w_{i,\text{gas,s}}$ is the gas species mass fraction of species i at the droplet surface and is determined using the vapour pressure p_{vap} of species i at the droplet surface. Moreover, the film factor is assumed to be 1/3, while larger values up to one result in increased vaporisation rates that are not in agreement with experimental observations [4,11,96].

In contrast to the classical vaporisation model, the model of Abramzon and Sirignano takes into account the thickening of the laminar boundary layer due to Stefan flow [11] and uses a modified Sherwood number at film condition [11]

$$Sh_{\text{film,mod}} = 2 + \frac{Sh_{\text{film},0} - 2}{F_{\text{m}}} \tag{13}$$

and a modified Nusselt number at film condition [11]

$$Nu_{\text{film,mod}} = 2 + \frac{Nu_{\text{film},0} - 2}{F_{\text{T}}}\,, \tag{14}$$

where $Sh_{\text{film},0}$ is the Sherwood number and $Nu_{\text{film},0}$ is the Nusselt number, each based on the Ranz–Marshall correlation [97,98], and F_{m} and F_{T} are correction factors for mass transfer and heat transfer. The Sherwood number $Sh_{\text{film},0}$ and the Nusselt number $Nu_{\text{film},0}$ are calculated by [97,98]

$$Sh_{\text{film},0} = 2 + 0.6\, Re_{\text{film}}^{1/2}\, Sc_{\text{film}}^{1/3}\,, \tag{15}$$

$$Nu_{\text{film},0} = 2 + 0.6\, Re_{\text{film}}^{1/2}\, Pr_{\text{film}}^{1/3}\,, \tag{16}$$

where Re_{film} is the Reynolds number, Sc_{film} is the Schmidt number and Pr_{film} is the Prandtl number, each calculated at film condition.

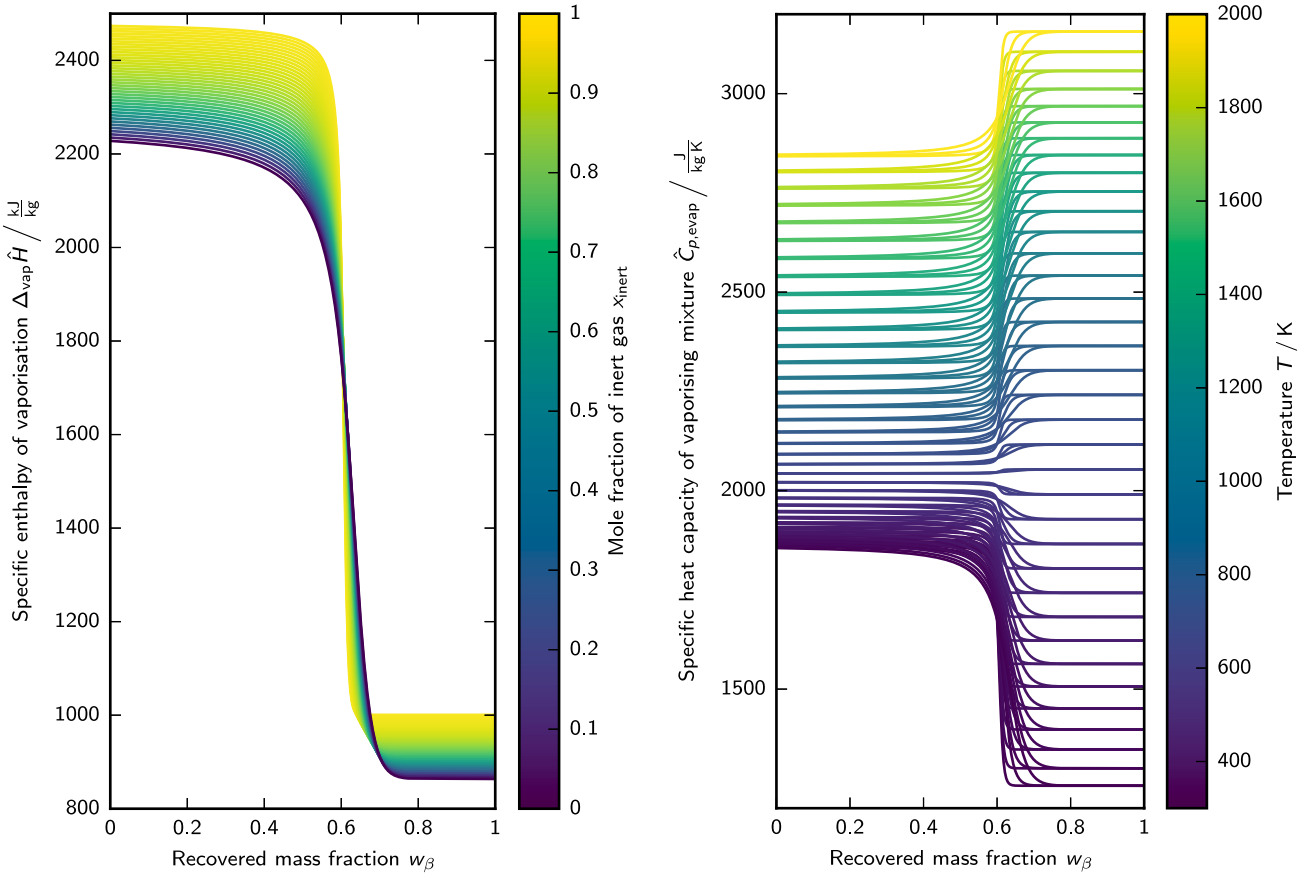

Fig. 5. Tabulated curves of the specific enthalpy of vaporisation of the vaporising mixture $\Delta_{vap}\hat{H}$ (left) and of the specific heat capacity of the vaporising mixture $\hat{C}_{p,evap}$ (right) for the ethylene glycol–water mixture. For reasons of clarity, only a few curves corresponding to the mole fractions of vapour are depicted for each temperature. (For interpretation of the references to colour in this figure, the reader is referred to the web version of this article.)

The correction factor for mass transfer F_m and the correction factor for heat transfer F_T are approximated by [11]

$$F_m = \begin{cases} (1+B_m)^{0.7}\,, & \text{if} \quad B_m = 0 \\ (1+B_m)^{0.7}\,\ln\left(\frac{1+B_m}{B_m}\right), & \text{else} \end{cases}, \tag{17}$$

$$F_T = \begin{cases} (1+B_T)^{0.7}\,, & \text{if} \quad B_T = 0 \\ (1+B_T)^{0.7}\,\ln\left(\frac{1+B_T}{B_T}\right), & \text{else} \end{cases}, \tag{18}$$

where B_m is the Spalding mass transfer number and B_T is the Spalding heat transfer number. The Spalding numbers B_m and B_T are defined by [11,94]

$$B_m = \frac{w_{vap,gas,s} - w_{vap,gas}}{1 + w_{vap,gas,s}}\,, \tag{19}$$

$$B_T = (1+B_m)^{\varphi} - 1\,, \tag{20}$$

where $w_{vap,gas,s}$ is the (total) gas species mass fraction of vapour at the droplet surface and $w_{vap,gas}$ is the (total) gas species mass fraction of vapour in the bulk and φ is an auxiliary model parameter. The gas species mass fractions $w_{vap,gas,s}$ and $w_{vap,gas}$ are equal to the mass fractions of the vaporising species in the case of single-component vaporisation and are the respective sums of the mass fractions of all vaporising species in the case of multi-component vaporisation. The auxiliary model parameter φ is defined by

$$\varphi = \frac{1}{Le_{film}}\,\frac{Sh_{film,mod}}{Nu_{film,mod}}\,\frac{\hat{C}_{p,vap,film}}{\hat{C}_{p,gas,film}}\,, \tag{21}$$

where Le_{film} is the Lewis number at film condition, $\hat{C}_{p,vap,film}$ is the specific vapour heat capacity at film condition and $\hat{C}_{p,gas,film}$ is the specific gas heat capacity at film condition. The Lewis number at film condition is defined by

$$Le_{film} = \frac{\lambda_{gas,film}}{\rho_{gas,film}\,\hat{C}_{p,gas,film}\,D_{gas,film}}\,, \tag{22}$$

where $\lambda_{gas,film}$ is the gas thermal conductivity, $\rho_{gas,film}$ is the gas density and $D_{gas,film}$ is an effective gas diffusion coefficient, each evaluated at film condition.

The modified Sherwood number at film condition $Sh_{film,mod}$ and the modified Nusselt number at film condition $Nu_{film,mod}$ are dimensionless auxiliary numbers. The (actual) Sherwood number at film condition Sh_{film} is defined by [11]

$$Sh_{film} = \begin{cases} Sh_{film,mod}\,, & \text{if} \quad B_m = 0 \\ Sh_{film,mod}\,\ln\left(\frac{1+B_m}{B_m}\right), & \text{else} \end{cases}, \tag{23}$$

and the (actual) Nusselt number at film condition Nu_{film} is calculated by

$$Nu_{film} = \begin{cases} Nu_{film,mod}\,, & \text{if} \quad B_T = 0 \\ Nu_{film,mod}\,\ln\left(\frac{1+B_T}{B_T}\right), & \text{else} \end{cases}. \tag{24}$$

The droplet has an initial mass $m_{liq,0}$, an initial temperature $T_{liq,0}$, an initial composition in mass fractions $\boldsymbol{w}_{liq,0}$ (or in mole fractions $\boldsymbol{x}_{liq,0}$) and an initial diameter $d_{liq,0}$. The model subsequently predicts the

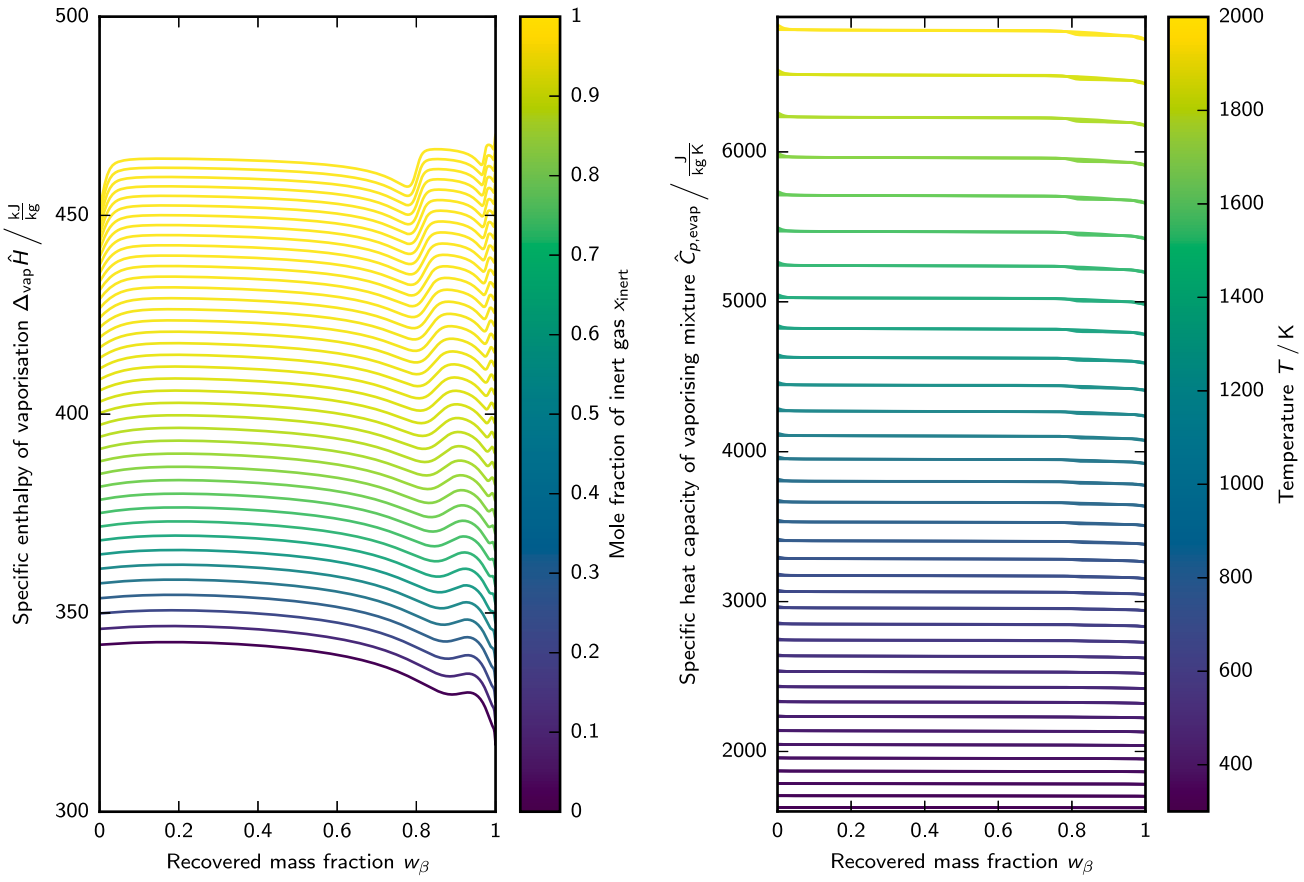

Fig. 6. Tabulated curves of the specific enthalpy of vaporisation of the vaporising mixture $\Delta_{vap}\hat{H}$ (left) and of the specific heat capacity of the vaporising mixture $\hat{C}_{p,evap}$ (right) for AtJ. For reasons of clarity, only a few curves corresponding to the mole fractions of vapour are depicted for each temperature. (For interpretation of the references to colour in this figure, the reader is referred to the web version of this article.)

droplet mass m_{liq}, the droplet temperature T_{liq}, the droplet composition in mass fractions $\boldsymbol{w}_{liq}$ and the droplet diameter d_{liq}. The mass transfer rate between droplet and gas phase is described by

$$\frac{dm_{liq}}{dt} = -\frac{A_{s,liq}\,\rho_{gas,film}\,D_{gas,film}}{d_{liq}}\,Sh_{film,mod}\,\ln\left(1+B_m\right)\,, \tag{25}$$

where $A_{s,liq}$ is the droplet surface area. The mass transfer rate of species i between droplet and gas phase is given by

$$\frac{dm_{i,liq}}{dt} = \varepsilon_i\,\frac{dm_{liq}}{dt}\,, \tag{26}$$

where $m_{i,liq}$ is the droplet mass of species i and ε_i is the vaporisation mass fraction of species i. The droplet composition in mass fractions $\boldsymbol{w} = (w_{i,liq})$ is defined by

$$w_{i,liq} = \frac{m_{i,liq}}{m_{liq}}\,, \tag{27}$$

while the composition of the vaporising mixture $\boldsymbol{\varepsilon} = (\varepsilon_i)$ is described by [14]

$$\varepsilon_i = w_{i,gas,s} + \frac{w_{i,gas,s} - w_{i,gas}}{B_m}\,. \tag{28}$$

The composition of the vaporising mixture $\boldsymbol{\varepsilon} = (\varepsilon_i)$ is also applied to determine the physical properties at film condition (see also Section 3.4).

The heat transfer between droplet and gas phase neglects the pressure change work, the pressure dependency of enthalpy and radiative heat transfer. The heat transfer rate is described by

$$m_{liq}\,\hat{C}_{p,liq}\,\frac{dT_{liq}}{dt} = A_{s,liq}\left(h_{conv,liq}\left(T_{gas}-T_{liq}\right) - \frac{dm_{liq}}{dt}\,\Delta_{vap}\hat{H}\right)\,, \tag{29}$$

where $h_{conv,liq}$ is the convective heat transfer coefficient and $\Delta_{vap}\hat{H}$ is the specific enthalpy of vaporisation. The latter is calculated using the vaporisation mass fractions $\boldsymbol{\varepsilon} = (\varepsilon_i)$. The convective heat transfer coefficient $h_{conv,liq}$ is calculated by

$$h_{conv,liq} = \frac{Nu_{film}\,\lambda_{gas,film}}{d_{liq}}\,, \tag{30}$$

where $\lambda_{gas,film}$ is the gas thermal conductivity at film condition. The droplet diameter d_{liq} is obtained by

$$d_{liq} = \left(\frac{6}{\pi}\,\frac{m_{liq}}{\rho_{liq}}\right)^{1/3}\,. \tag{31}$$

4.3. Absolute deviations, relative deviations and integral deviations

The predictions based on a TDC model are compared with the predictions based on a DC model using absolute deviations AD, relative deviations RD, integral deviations ID, droplet lifetime differences $\Delta t_{liq,max}$ and maximum droplet temperature differences $\Delta T_{liq,max}$. The DC models were applied as reference models and account for all species prevailing in the respective mixtures. The absolute deviations AD and the relative deviations RD are given by

$$AD_X = X|_{TDC} - X|_{DC}\,, \tag{32}$$

$$\mathrm{RD}_X = \frac{X|_{\mathrm{TDC}} - X|_{\mathrm{DC}}}{X|_{\mathrm{DC}}}, \tag{33}$$

where X is an arbitrary quantity (such as the droplet position x_{liq}, the droplet velocity u_{liq}, the droplet temperature T_{liq} or the droplet diameter d_{liq}), TDC refers to the results based on a tabulated distillation curve model and DC refers to the results based on a discrete component model.

The integral deviations for predictions of droplet position $\mathrm{ID_x}$, droplet velocity $\mathrm{ID_u}$, droplet temperature $\mathrm{ID_T}$ and droplet diameter $\mathrm{ID_d}$ are defined by

$$\mathrm{ID_x} = \frac{\int_0^{t_{\mathrm{liq,max}}} x_{\mathrm{liq}}\big|_{\mathrm{TDC}} - x_{\mathrm{liq}}\big|_{\mathrm{DC}}\,\mathrm{d}t}{\int_0^{t_{\mathrm{liq,max}}} x_{\mathrm{liq}}\big|_{\mathrm{DC}}\,\mathrm{d}t}, \tag{34}$$

$$\mathrm{ID_u} = \frac{\int_0^{t_{\mathrm{liq,max}}} u_{\mathrm{liq}}\big|_{\mathrm{TDC}} - u_{\mathrm{liq}}\big|_{\mathrm{DC}}\,\mathrm{d}t}{\int_0^{t_{\mathrm{liq,max}}} u_{\mathrm{liq}}\big|_{\mathrm{DC}}\,\mathrm{d}t}, \tag{35}$$

$$\mathrm{ID_T} = \frac{\int_0^{t_{\mathrm{liq,max}}} T_{\mathrm{liq}}\big|_{\mathrm{TDC}} - T_{\mathrm{liq}}\big|_{\mathrm{DC}}\,\mathrm{d}t}{\int_0^{t_{\mathrm{liq,max}}} T_{\mathrm{liq}}\big|_{\mathrm{DC}}\,\mathrm{d}t}, \tag{36}$$

$$\mathrm{ID_d} = \frac{\int_0^{t_{\mathrm{liq,max}}} d_{\mathrm{liq}}\big|_{\mathrm{TDC}} - d_{\mathrm{liq}}\big|_{\mathrm{DC}}\,\mathrm{d}t}{\int_0^{t_{\mathrm{liq,max}}} d_{\mathrm{liq}}\big|_{\mathrm{DC}}\,\mathrm{d}t}, \tag{37}$$

where the droplet lifetime

$$t_{\mathrm{liq,max}} = \min\left(t_{\mathrm{liq,max}}\big|_{\mathrm{TDC}}, t_{\mathrm{liq,max}}\big|_{\mathrm{DC}}\right) \tag{38}$$

is used as an upper integration bound. The droplet lifetime differences $\Delta t_{\mathrm{liq,max}}$ and the maximum droplet temperature differences $\Delta T_{\mathrm{liq,max}}$ are defined by

$$\Delta t_{\mathrm{liq,max}} = t_{\mathrm{liq,max}}\big|_{\mathrm{TDC}} - t_{\mathrm{liq,max}}\big|_{\mathrm{DC}}, \tag{39}$$

$$\Delta T_{\mathrm{liq,max}} = \max\left(T_{\mathrm{liq}}\big|_{\mathrm{TDC}} - T_{\mathrm{liq}}\big|_{\mathrm{DC}}\right). \tag{40}$$

5. Discussion

Single-droplet vaporisation simulations were carried out for the verification, analysis and validation of TDC models. The accuracy and the efficiency of TDC models are discussed in Sections 5.1 and 5.2. The effects of (i) internal heat and mass transfer, (ii) tabulation and time step and (iii) physical property models are analysed in Sections 5.3, 5.4 and 5.5. The predictions are compared with measured data in Section 5.6, while the differences between distillation curve and TDC models and the limitations of TDC models are finally discussed in Sections 5.7 and 5.8.

5.1. Accuracy of tabulated distillation curve models

The accuracy of TDC models is presented for nonane, the ethylene glycol–water mixture and AtJ (see Section 3.6) considering three test cases.

In test case 1, an initially non-moving spherical droplet with an initial temperature of 300 K and an initial diameter of 100 µm is considered in a stationary, moving gas phase consisting of nitrogen with a velocity of 2 m/s and a temperature of 950 K at a constant pressure of 1 bar. In test case 2, the gas temperature is increased to 1400 K. In test case 3, the initial droplet diameter is changed to 200 µm. The initial droplet diameters $d_{\mathrm{liq,0}}$, initial droplet temperatures $T_{\mathrm{liq,0}}$ and gas temperatures T_{gas} of the test cases are summarised in Table 3. The single-droplet vaporisation simulations were conducted using constant time steps of 10^{-2} ms and baseline tabulations for the TDC models (see also Section 5.4).

The simulated droplet temperatures are shown for the three mixtures and the three test cases in Figs. 7–9, while the simulated droplet velocities and the simulated droplet diameters are shown in Figs. S13–S21. In Figs. 7–9, the predictions based on the DC models are depicted as coloured lines, while the results based on the TDC models are shown as dashed lines. The curves completely overlap, which indicates the necessity of absolute deviations AD or relative deviations RD as quality measures (see Section 4.3). The absolute deviations are used for the

Table 3
Initial droplet diameters $d_{\mathrm{liq,0}}$, initial droplet temperatures $T_{\mathrm{liq,0}}$ and gas temperatures T_{gas} of the test cases.

Test case	$\frac{d_{\mathrm{liq,0}}}{\mu\mathrm{m}}$	$\frac{T_{\mathrm{liq,0}}}{\mathrm{K}}$	$\frac{T_{\mathrm{gas}}}{\mathrm{K}}$
1	100	300	950
2	100	300	1400
3	200	300	950

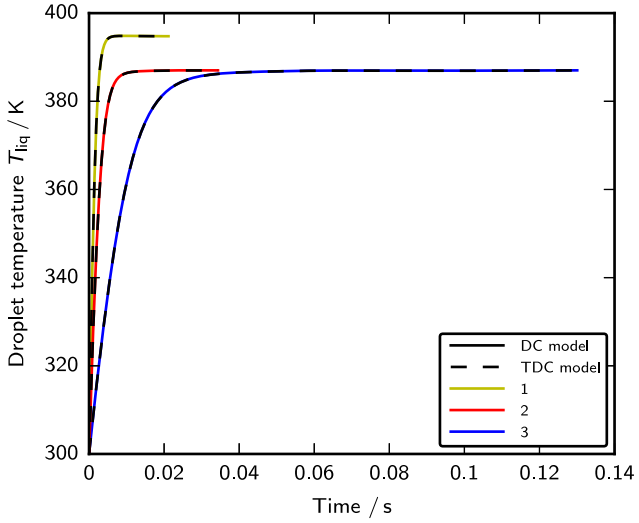

Fig. 7. Droplet temperatures T_{liq}: predictions based on DC and TDC models for nonane and test cases 1, 2 and 3. (For interpretation of the references to colour in this figure, the reader is referred to the web version of this article.)

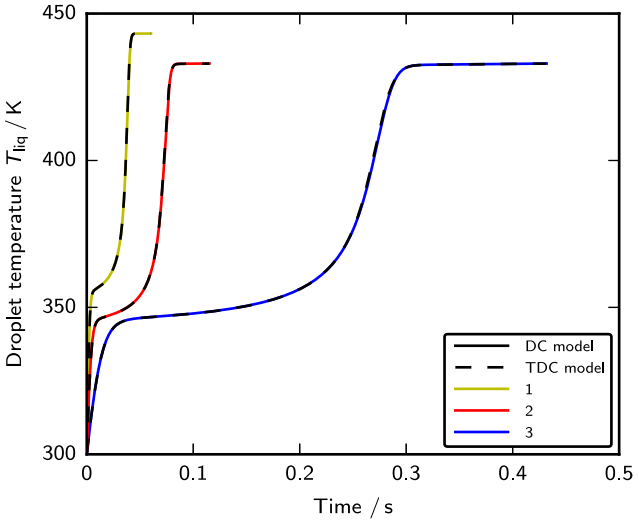

Fig. 8. Droplet temperatures T_{liq}: predictions based on DC and TDC models for the ethylene glycol–water mixture and test cases 1, 2 and 3. (For interpretation of the references to colour in this figure, the reader is referred to the web version of this article.)

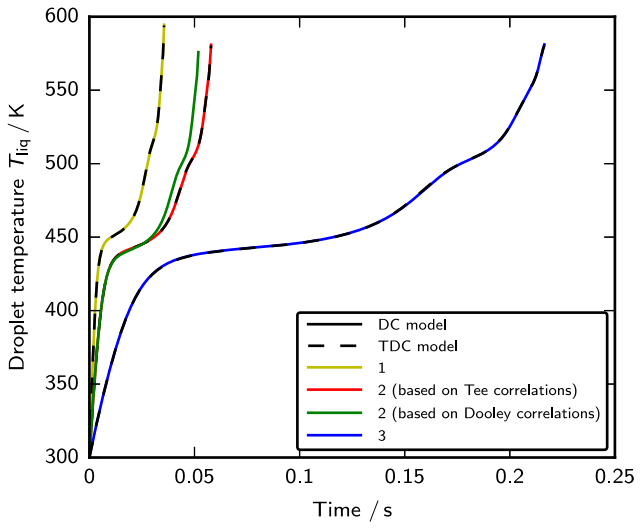

Fig. 9. Droplet temperatures T_{liq}: predictions based on DC and TDC models for AtJ and test cases 1, 2 and 3. (For interpretation of the references to colour in this figure, the reader is referred to the web version of this article.)

temperatures, while the relative deviations are applied to the other quantities.

The absolute deviations for the droplet temperature predictions are shown in Figs. 10–12 (each at the centre) and are between −2 K and 2 K. These deviations can be accepted and are mainly connected with non-linear relationships in the vaporisation model, such as the non-linear mixing rules for dynamic liquid viscosity and liquid thermal conductivity. Therefore, the deviations are typically larger for liquid mixtures with species whose liquid thermal conductivities are quite different at constant temperature.

The relative deviations for the droplet velocity and droplet diameter predictions are shown in Figs. 10–12 (each on the left side and the right side, respectively). These deviations are mainly small. Larger deviations for the droplet diameter predictions are only found for the final vaporisation stages due to different droplet life times.

The relative deviations for the vapour pressure predictions are shown in Figs. 13–15 (each on the left side) demonstrating again quite small relative deviations between the simulation results. Some larger relative deviations are observed for the initial vaporisation stages and in the presence of strong composition changes. Furthermore, note that the vapour pressure was bounded by a minimum value of 10^{-2} kPa for nonane, by a minimum value of 1 kPa for the ethylene glycol–water mixture and by a minimum value of 10^{-2} kPa for AtJ, as minimum mole fractions of vapour of 10^{-4}, 10^{-2} and 10^{-4}, respectively, were used for the tabulations (see Section 3.6), resulting in higher relative deviations at the initial vaporisation stages.

Finally, the relative deviations for Spalding heat transfer number predictions are compared in Figs. 13–15 (each at the centre). The Spalding heat transfer number B_T is calculated using various physical properties (see Eqs. (19)–(21)). Therefore, its prediction can be affected more strongly by model errors compared to the individual physical properties. However, the relative deviations are up to 6% only and are at largest for the bi-component mixture, which is because of the strong changes of the liquid thermal conductivity during vaporisation. Therefore, TDC models have provided excellent predictions compared to discrete component models.

5.2. Computing times of tabulated distillation curve models

The droplet models were incorporated in an in-house software in Python. This software enables rapid testing of new models or new implementations at various conditions but has also a huge overload of methods and outputs. This is appreciated for tests but increases the computing times of simulations. Therefore, the efficiency of TDC models was only investigated in a first approximation in this study. The results showed that, for any multi-component liquid, TDC models (based on the baseline tabulation) require similar computing times as DC models with approximately eight components. TDC models for mixtures with dozens or even hundreds of species are thus significantly more efficient than DC models at a similar level of accuracy. Future studies may provide a more detailed analysis.

5.3. Effect of internal heat and mass transfer

Uniform distributions of droplet temperature and droplet species concentrations are assumed for the TDC models (in line with ITC/ID models). Thus, internal heat and mass transfer is neglected in contrast to ETC/ED models or distillation curve models. However, in order to show the possible impact of internal heat and mass transfer, the distillation Peclet number Pe_{dist} (see Section S3) has been determined using the mass transfer rate between droplet and gas phase dm_{liq}/dt, the droplet density ρ_{liq} and a constant effective droplet diffusion coefficient $D_{liq,eff}$. The mass transfer rate between droplet and gas phase dm_{liq}/dt and the droplet density ρ_{liq} were obtained from the droplet vaporisation simulation results. The effective droplet diffusion coefficient $D_{liq,eff}$, in turn, was assumed by a value of 10^{-9} m^2/s, which is the typical magnitude of diffusion coefficients in low-viscous multi-component liquids. It is expected that this approach is sufficient to determine the magnitude of the distillation Peclet number Pe_{dist}.

The distillation Peclet numbers Pe_{dist} are shown for the ethylene glycol–water mixture in Fig. 14 and for AtJ in Fig. 15 (each on the right side). The distillation Peclet numbers Pe_{dist} are significantly larger than one, which indicates a large impact of internal mass transfer. Therefore, internal heat and mass transfer should not be neglected even though it is a common approach for large-scale CFD simulations. Future studies may develop approaches based on TDC models and distillation curve models to account for internal heat and mass transfer (see Eq. S14).

5.4. Effect of tabulation and time step

The single-droplet vaporisation predictions presented in Section 5.1 were obtained using the baseline tabulation and constant time steps of 10^{-2} ms. However, for test case 2, additional simulations were performed (i) using the coarse or the fine tabulation and (ii) using constant time steps of 1 ms, 10^{-1} ms or 10^{-3} ms. The integral deviations for predictions of droplet position ID_x, droplet velocity ID_u, droplet temperature ID_T and droplet diameter ID_d are compared for the bi-component mixture in Table 5 and for the technical fuel in Table 6.

The results show that (i) the droplet lifetimes $t_{liq,max}$ and the droplet temperatures T_{liq} are well predicted for all tabulations using constant time steps below 10^{-1} ms and (ii) the integral deviations usually do not decrease with a decrease in time step below 10^{-1} ms. In particular, constant time steps of 10^{-3} ms do not significantly improve the predictions based on TDC models compared to constant time steps of 10^{-2} ms. Therefore, the accuracy of the simulation results is restricted equally by the time step and by the tabulated distillation curve data. Furthermore, the integral deviations for droplet diameter predictions ID_d mainly decrease with improved tabulation at constant time step, while similar effects are not observed for the integral deviations for predictions of droplet position ID_x, droplet velocity ID_u and droplet temperature ID_T. Therefore, the baseline tabulation and constant time steps of 10^{-2} ms have been appropriate for the single-droplet vaporisation simulations using TDC models presented in Section 5.1 and are recommended for future studies.

The results also demonstrate that single-droplet vaporisation simulations using TDC models can be performed for a wide range of time steps between 10^{-3} ms and 1 ms without any challenges. This is primarily because constant values are assigned outside the tabulated data, which, in turn, provides numerical stability. Larger numerical deviations might be only observed for the final vaporisation stages.

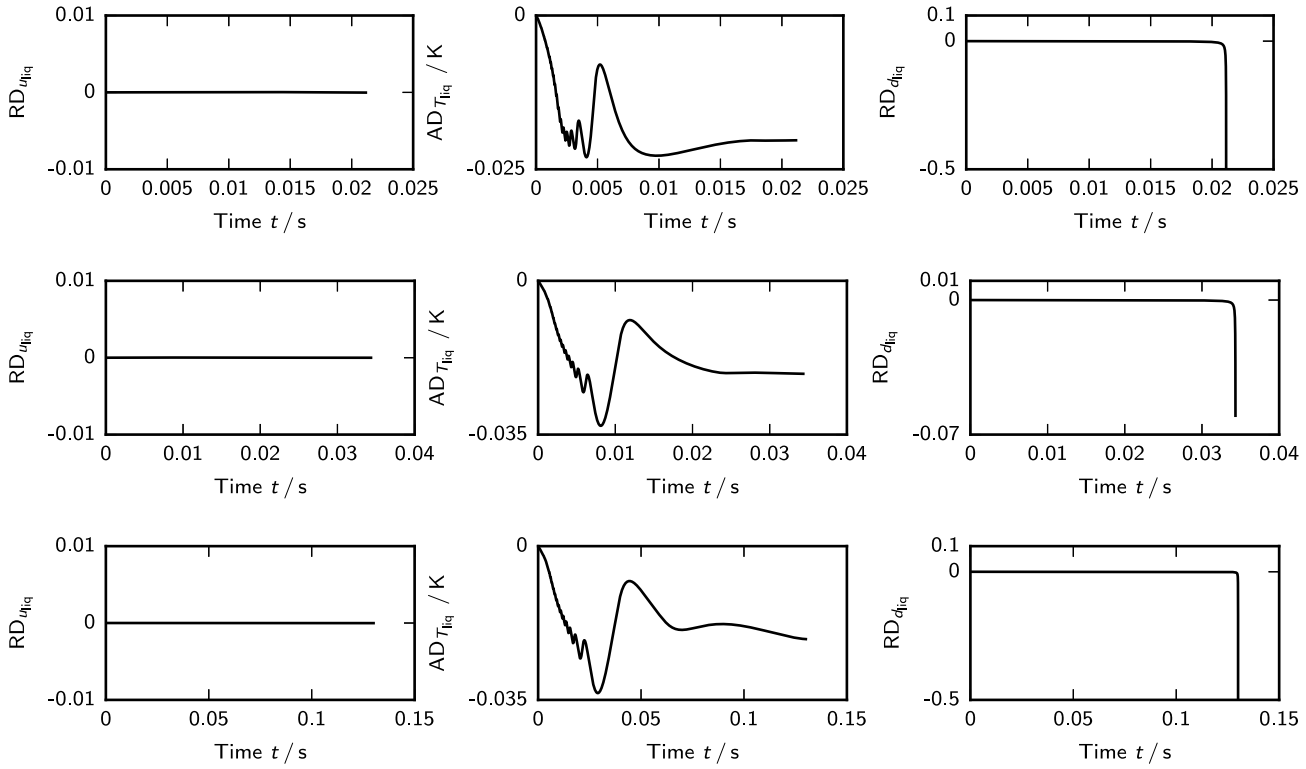

Fig. 10. Relative deviations for droplet velocity predictions $RD_{u_{liq}}$ (left), absolute deviations for droplet temperature predictions $AD_{T_{liq}}$ (centre) and relative deviations for droplet diameter predictions $RD_{d_{liq}}$ (right), each obtained for nonane and test cases 1 (top), 2 (centre) and 3 (bottom).

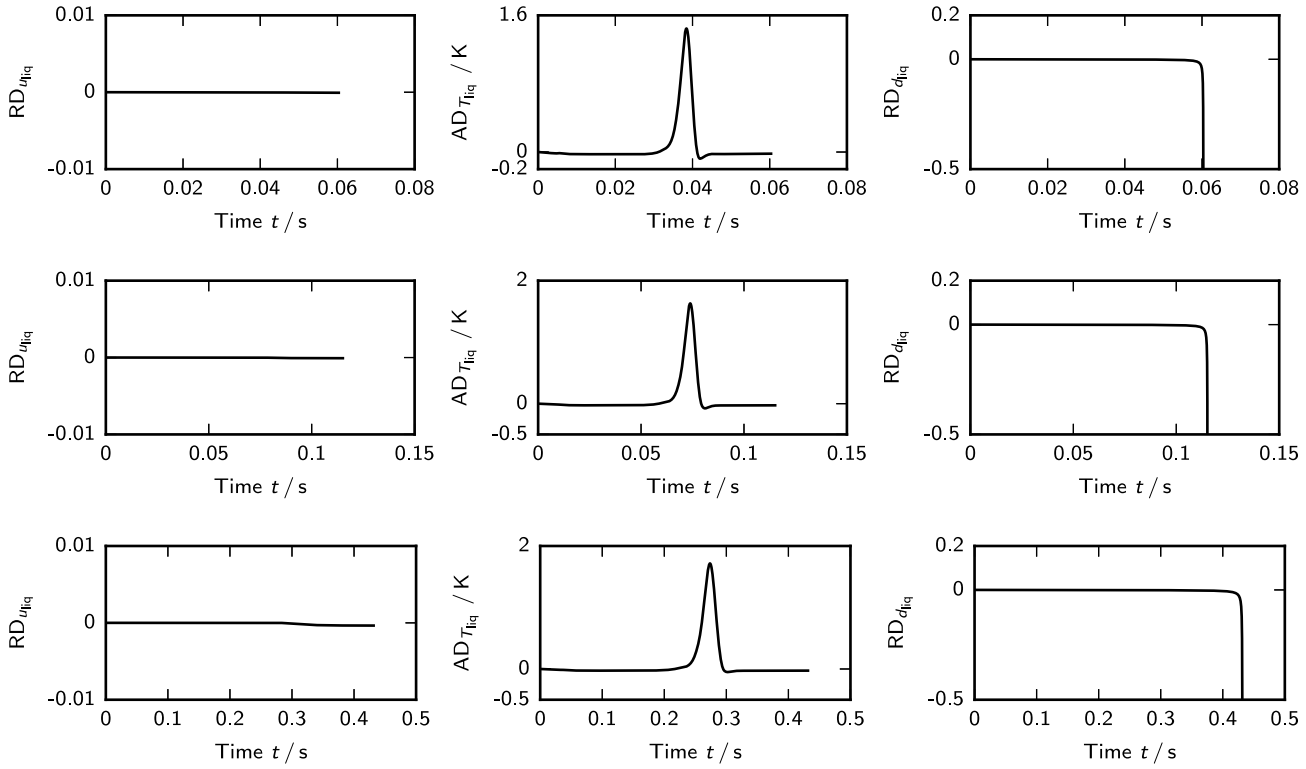

Fig. 11. Relative deviations for droplet velocity predictions $RD_{u_{liq}}$ (left), absolute deviations for droplet temperature predictions $AD_{T_{liq}}$ (centre) and relative deviations for droplet diameter predictions $RD_{d_{liq}}$ (right), each obtained for the ethylene glycol–water mixture and test cases 1 (top), 2 (centre) and 3 (bottom).

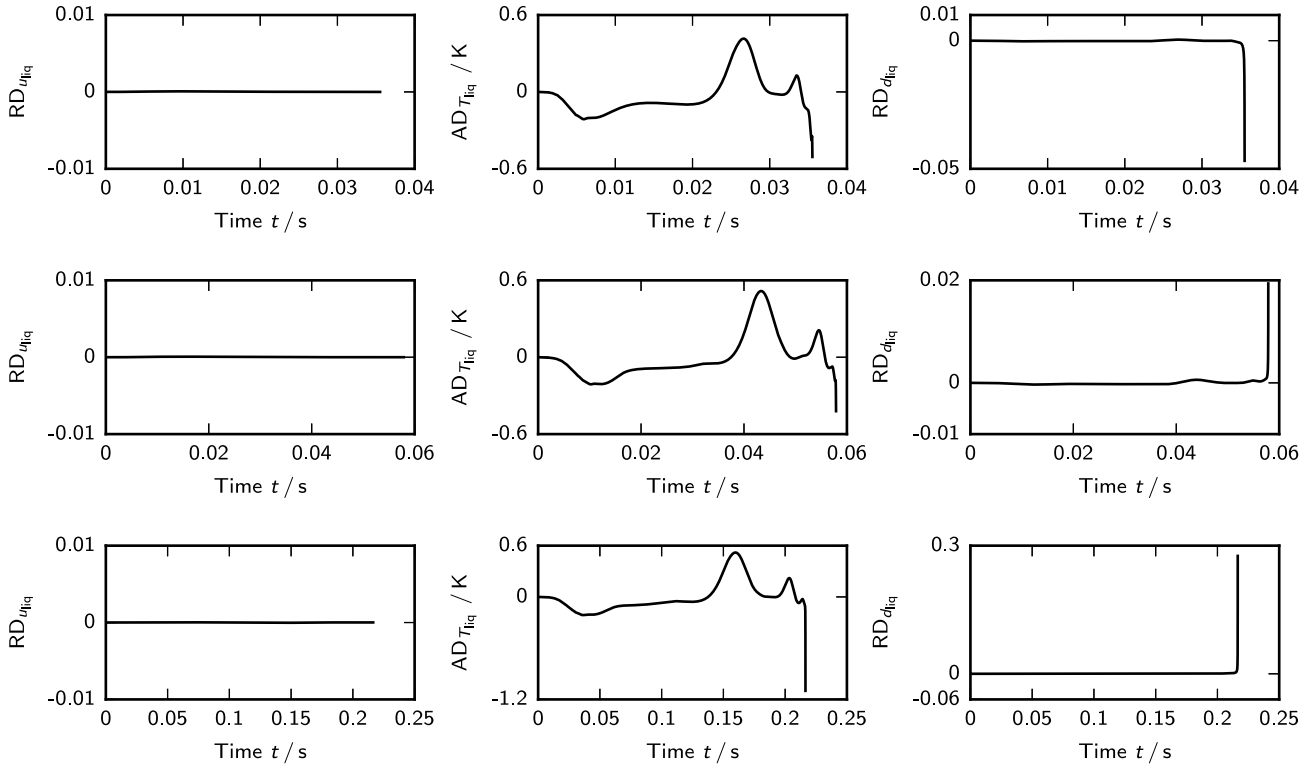

Fig. 12. Relative deviations for droplet velocity predictions $RD_{u_{liq}}$ (left), absolute deviations for droplet temperature predictions $AD_{T_{liq}}$ (centre) and relative deviations for droplet diameter predictions $RD_{d_{liq}}$ (right), each obtained for AtJ and test cases 1 (top), 2 (centre) and 3 (bottom).

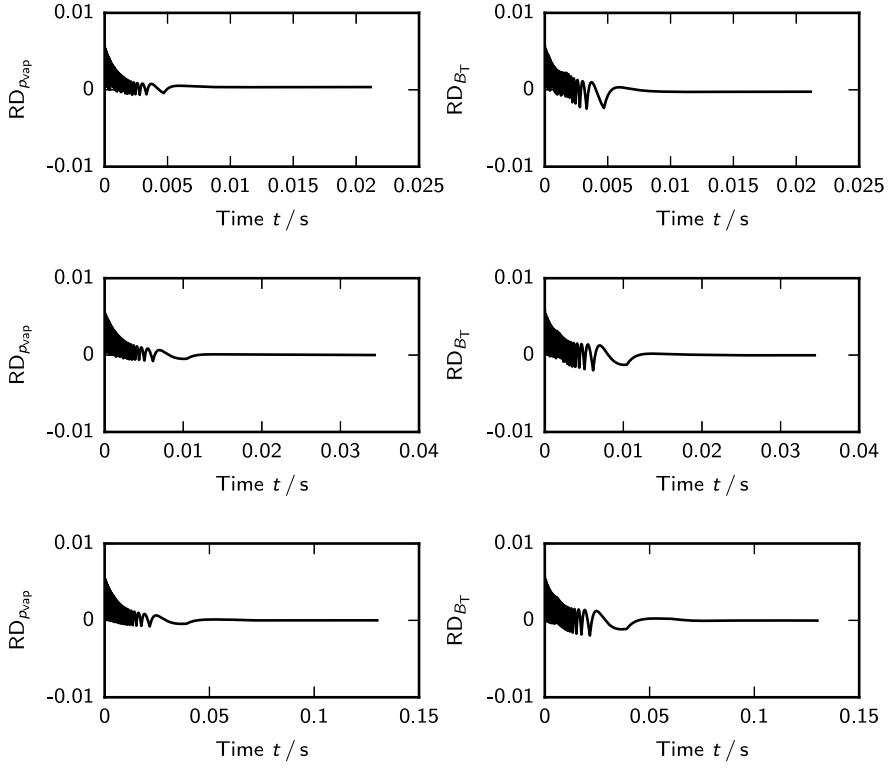

Fig. 13. Relative deviations for vapour pressure predictions $RD_{p_{vap}}$ (left) and for Spalding heat transfer number predictions RD_{B_T} (centre), each obtained for nonane and test cases 1 (top), 2 (centre) and 3 (bottom).

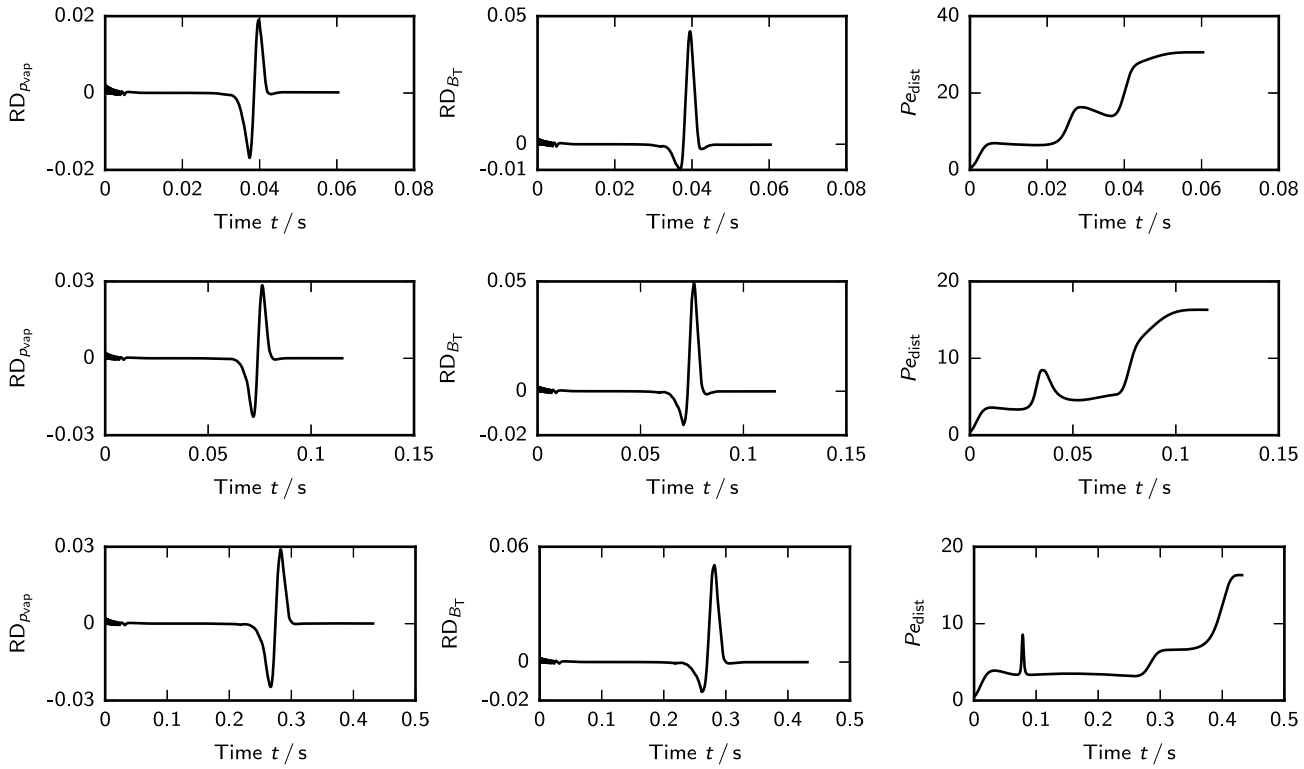

Fig. 14. Relative deviations for vapour pressure predictions $RD_{p_{vap}}$ (left) and for Spalding heat transfer number predictions RD_{B_T} (centre) as well as distillation Peclet numbers Pe_{dist} (right), each obtained for the ethylene glycol–water mixture and test cases 1 (top), 2 (centre) and 3 (bottom).

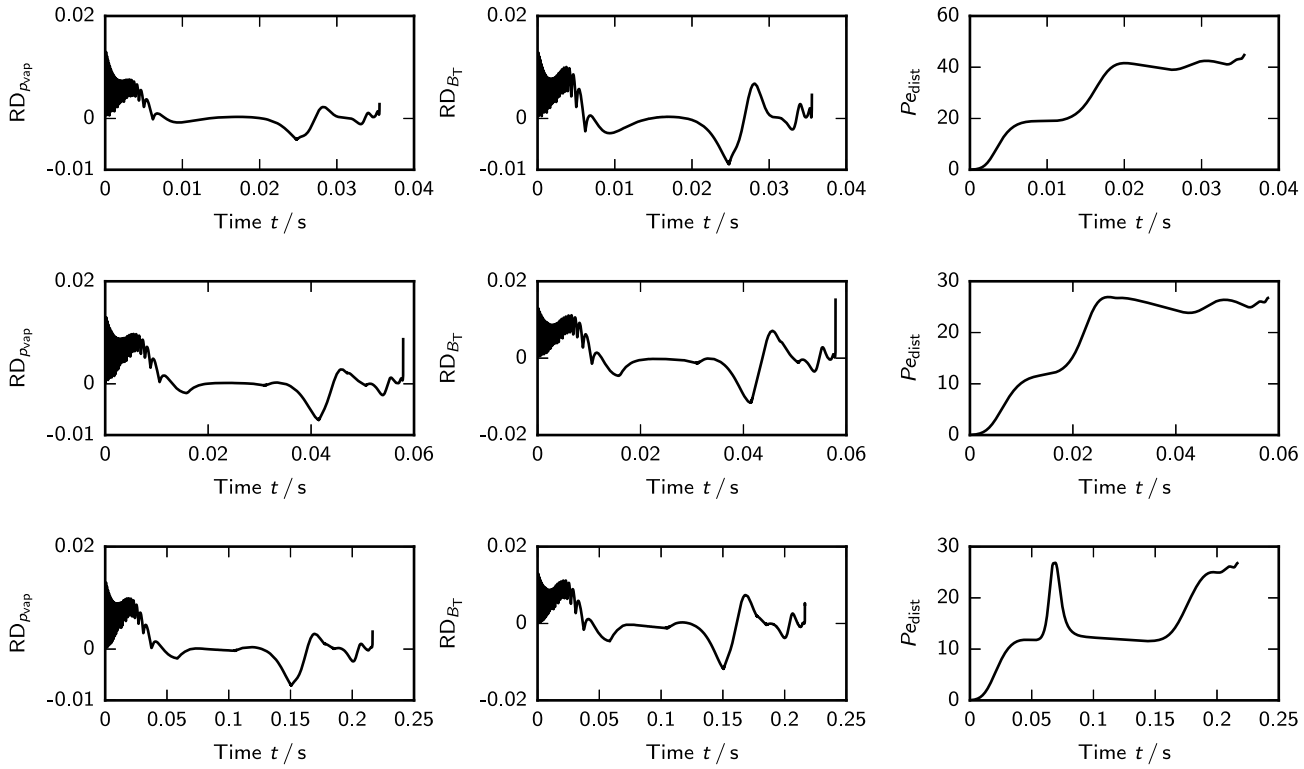

Fig. 15. Relative deviations for vapour pressure predictions $RD_{p_{vap}}$ (left) and for Spalding heat transfer number predictions RD_{B_T} (centre) as well as distillation Peclet numbers Pe_{dist} (right), each obtained for AtJ and test cases 1 (top), 2 (centre) and 3 (bottom).

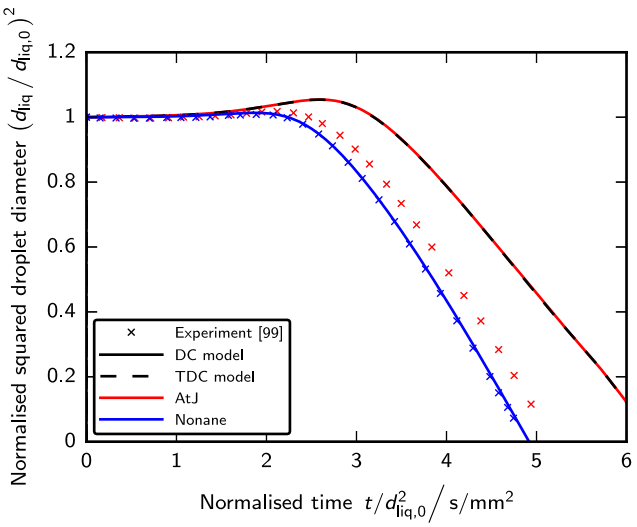

Fig. 16. Normalised squared droplet diameters $\left(d_{\mathrm{liq}}/d_{\mathrm{liq},0}\right)^2$: experimental data from microscopic double-pulse shadowgraphy measurements in free-falling droplet experiments [99] and predictions based on DC and TDC models for nonane and AtJ and accounting for the experimental conditions.

5.5. Effect of physical property models

The single-droplet vaporisation simulations were conducted using fixed sets of physical property models. For example, considering set B, the characteristic Lennard–Jones length of the vapour σ_{vap} and the characteristic Lennard–Jones energy parameter of the vapour related to the Boltzmann constant $\epsilon_{\mathrm{vap}}/k_{\mathrm{B}}$ were calculated using the van der Waals mixing rule and the Tee correlations [88]. However, the Dooley correlations [100] may be used instead of the Tee correlations [88]. In order to show the impact of physical property models on the predictions, single-droplet vaporisation simulations were conducted based on the discrete component model and the Dooley correlations [100] and considering the liquid technical fuel AtJ and test case 2. The predictions are depicted in Fig. 9 and show the strong impact of a single physical property model on the predictions (see Section 2.2). Therefore, physical property models induce uncertainties that can be larger than those of TDC models. Furthermore, the comparison shows that physical property models should be carefully chosen for TDC models, as wrongly selected models may require an elaborative re-generation of the thermodynamic state and physical property tables or might result in an unfair comparison with DC models.

5.6. Comparison with experimental data

Predictions based on DC models were employed in Section 5.1 to verify the predictions based on TDC models, where DC models were considered as reference models in agreement with previous studies [52]. However, the vaporisation of several surrogate and technical fuels, including nonane and AtJ, was recently investigated using free-falling droplets and microscopic double-pulse shadowgraphy measurements in a laminar flow channel [99]. The gas temperatures were up to 1300 K, while the free-falling droplets exhibited initial diameters of 77 µm and axial velocities between 0.75 m/s and 1 m/s [99]. For nonane and AtJ, additional single-droplet vaporisation simulations were conducted assuming the measured initial droplet diameters and the derived profiles for axial gas temperature and droplet velocity [99]. The predictions are compared with the experimental data using the normalised squared droplet diameter $\left(d_{\mathrm{liq}}/d_{\mathrm{liq},0}\right)^2$ and the normalised time $t/d_{\mathrm{liq},0}^2$ in Fig. 16. For nonane, the predictions are in excellent agreement with the experimental data, whereas large deviations between measured and predicted data are found for AtJ. The technical fuel has shown much higher vaporisation rates in the experiments than predicted by both DC and TDC models, which is in agreement with the deviations between the experimental and numerical distillation curves (see Section 2.2.4). The deviations are therefore linked to inappropriate physical property data. Neither DC nor TDC models can overcome such deficiencies.

5.7. Comparison of tabulated distillation curve models with distillation curve models

Distillation curve models and tabulated distillation curve models are both named after distillation curves. This suggests that both modelling approaches have significant similarities. However, both approaches are based on different methods. For example, distillation curve models mimic the experimental distillation behaviour based on experimental distillation data and empirical approaches, whereas tabulated distillation models describe the theoretical distillation behaviour based on numerical equilibrium distillation curves. Therefore, distillation curve models might be referred to as *experimental distillation curve models*, while tabulated distillation curves might be described as *tabulated numerical distillation curve models*. The main differences are summarised in Table 4.

5.8. Limitations of tabulated distillation curve models

The single-droplet vaporisation simulations with TDC models have provided excellent results if compared to DC models and have been more efficient for liquids with more than eight components. This is beneficial for CFD simulations of large-scale systems with multi-component droplet vaporisation phenomena. However, the simulations have also shown various limitations which are summarised below:

1. Significant computing resources are required to generate and tabulate distillation and physical property curves. Therefore, these curves should be based on the most appropriate physical property data.
2. TDC models cannot provide excellent predictions of experiments when physical property data are inappropriate.
3. TDC models require high load times when reading the tables into memory. Therefore, neural networks may be employed instead, accepting a loss in accuracy but shortening computing times.
4. Isobaric conditions have been assumed to simplify pre-computations and tabulations as such conditions are applicable to most chemical and high-temperature processes.
5. Ideal vapour–liquid equilibria have been assumed to simplify the distillation calculations. However, TDC models are also applicable to non-ideal vapour–liquid equilibria.
6. TDC models neglect internal heat and mass transfer, which is questionable for larger droplets. Therefore, TDC models may be extended by new approaches based on previously underlined interpolation concepts [55].
7. TDC models were presented for three liquids and were tested for three atmospheric-pressure conditions. However, TDC models are applicable to a wide range of multi-component liquids and conditions.
8. TDC models were only employed in single-droplet simulations but may also be incorporated into CFD simulations of large-scale technical systems.

Table 4
Differences between distillation curve models and tabulated distillation curve models.

	Distillation curve models	Tabulated distillation curve models
Data basis	Experimental distillation data	Numerical equilibrium distillation data
Internal heat and mass transfer	Yes (based on interpolation)	No
Fluids	Jet fuels, diesel, gasoline	All liquids

Table 5
Set-ups and results of the single-droplet vaporisation simulations considering the ethylene glycol–water mixture and test case 2: time steps Δt, integral deviations ID_x, ID_u, ID_T and ID_d, droplet lifetimes $t_{liq,max}$, droplet lifetime differences $\Delta t_{liq,max}$, maximum droplet temperatures $T_{liq,max}$ and maximum droplet temperature differences $\Delta T_{liq,max}$.

Test case	Tabulation	Δt / ms	ID_x / %	ID_u / %	ID_T / %	ID_d / %	$t_{liq,max}$ / ms	$\Delta t_{liq,max}$ / ms	$T_{liq,max}$ / K	$\Delta T_{liq,max}$ / K
2	Coarse	1	0.003 12	0.004 94	−0.055 95	0.138 49	$1.14 \cdot 10^2$	1.0	432.99	0.00
2	Baseline	1	0.002 91	0.004 94	−0.045 00	0.144 60	$1.14 \cdot 10^2$	1.0	432.99	0.00
2	Fine	1	0.002 88	0.004 99	−0.040 74	0.147 53	$1.14 \cdot 10^2$	1.0	432.99	0.00
2	Coarse	10^{-1}	0.000 01	−0.001 63	0.001 38	−0.048 40	$1.15 \cdot 10^2$	$-1.0 \cdot 10^{-1}$	432.99	1.39
2	Baseline	10^{-1}	−0.000 27	−0.001 65	0.012 46	−0.042 56	$1.15 \cdot 10^2$	$-1.0 \cdot 10^{-1}$	432.99	1.41
2	Fine	10^{-1}	−0.000 31	−0.001 61	0.016 80	−0.040 13	$1.15 \cdot 10^2$	0.0	432.99	1.41
2	Coarse	10^{-2}	−0.000 29	−0.002 30	0.007 41	−0.064 78	$1.15 \cdot 10^2$	$-8.0 \cdot 10^{-2}$	432.99	1.61
2	Baseline	10^{-2}	−0.000 57	−0.002 33	0.018 49	−0.058 86	$1.15 \cdot 10^2$	$-8.0 \cdot 10^{-2}$	432.99	1.63
2	Fine	10^{-2}	−0.000 61	−0.002 29	0.022 84	−0.056 28	$1.15 \cdot 10^2$	$-7.0 \cdot 10^{-2}$	432.99	1.63
2	Coarse	10^{-3}	−0.000 34	−0.002 35	0.007 85	−0.065 67	$1.15 \cdot 10^2$	$-8.0 \cdot 10^{-2}$	432.99	1.63
2	Baseline	10^{-3}	−0.000 62	−0.002 38	0.018 92	−0.059 82	$1.15 \cdot 10^2$	$-7.7 \cdot 10^{-2}$	432.99	1.65
2	Fine	10^{-3}	−0.000 66	−0.002 34	0.023 27	−0.057 05	$1.15 \cdot 10^2$	$-7.5 \cdot 10^{-2}$	432.99	1.65

Table 6
Set-ups and results of the single-droplet vaporisation simulations considering AtJ and test case 2: time steps Δt, integral deviations ID_x, ID_u, ID_T and ID_d, droplet lifetimes $t_{liq,max}$, droplet lifetime differences $\Delta t_{liq,max}$, maximum droplet temperatures $T_{liq,max}$ and maximum droplet temperature differences $\Delta T_{liq,max}$.

Test case	Tabulation	Δt / ms	ID_x / %	ID_u / %	ID_T / %	ID_d / %	$t_{liq,max}$ / ms	$\Delta t_{liq,max}$ / ms	$T_{liq,max}$ / K	$\Delta T_{liq,max}$ / K
2	Coarse	1	0.006 34	0.000 47	−0.129 90	−0.296 10	$5.80 \cdot 10^1$	−1.0	647.39	54.26
2	Baseline	1	0.004 70	−0.000 36	−0.140 13	−0.282 98	$5.80 \cdot 10^1$	−1.0	647.39	47.68
2	Fine	1	0.004 20	−0.000 55	−0.127 57	−0.272 48	$5.80 \cdot 10^1$	−1.0	647.39	49.38
2	Coarse	10^{-1}	0.005 19	0.002 68	−0.038 91	−0.055 41	$5.78 \cdot 10^1$	0.0	579.46	0.36
2	Baseline	10^{-1}	0.003 33	0.001 78	−0.014 78	−0.033 59	$5.78 \cdot 10^1$	0.0	579.46	0.37
2	Fine	10^{-1}	0.002 77	0.001 56	−0.011 78	−0.023 72	$5.78 \cdot 10^1$	0.0	579.46	0.36
2	Coarse	10^{-2}	0.005 11	0.002 99	−0.025 62	−0.034 96	$5.79 \cdot 10^1$	$-1.0 \cdot 10^{-2}$	580.86	0.29
2	Baseline	10^{-2}	0.003 22	0.002 07	−0.001 38	−0.013 10	$5.79 \cdot 10^1$	0.0	580.86	0.52
2	Fine	10^{-2}	0.002 65	0.001 84	0.001 67	−0.003 31	$5.79 \cdot 10^1$	0.0	580.86	0.52
2	Coarse	10^{-3}	0.005 10	0.003 02	−0.024 21	−0.032 78	$5.79 \cdot 10^1$	$-4.0 \cdot 10^{-3}$	580.76	0.31
2	Baseline	10^{-3}	0.003 21	0.002 10	0.000 03	−0.011 04	$5.79 \cdot 10^1$	$3.0 \cdot 10^{-3}$	580.76	0.53
2	Fine	10^{-3}	0.002 63	0.001 87	0.003 10	−0.001 27	$5.79 \cdot 10^1$	$7.0 \cdot 10^{-3}$	580.76	0.53

6. Conclusions

A new approach was developed for an accurate and efficient mathematical description of the single-droplet vaporisation of complex technical fuels. This approach utilises the link between distillation and vaporisation, assumes rapid internal mixing and isobaric conditions and employs models based on tabulated equilibrium distillation and physical property curves. The models are referred to as tabulated distillation curve models and were derived for a pure liquid compound, a bi-component liquid and a liquid technical fuel assuming ideal atmospheric-pressure conditions.

Single-droplet vaporisation simulations showed that tabulated distillation curve models provide predictions that are in excellent agreement with results based on discrete component models and are more efficient for liquids with more than eight components. In addition, the simulations demonstrated, through the application to a liquid technical fuel, that tabulated distillation curve models are applicable to any liquid multi-component mixture if composition and physical property models are given. Therefore, tabulated distillation curve models can outperform surrogate, continuous thermodynamics, hybrid, quasi-discrete component and distillation curve models.

However, similarly to continuous thermodynamics or quasi-discrete component models, the accuracy of tabulated distillation curve models is restricted by the accuracy of mixture composition and physical property data. Therefore, future (experimental) studies should improve upon the physical property models, methods and databases for technical fuel compounds. In addition, the accuracy and efficiency of multi-component vaporisation simulations using tabulated distillation curve models may be investigated using CFD simulations.

Future studies should also apply tabulated distillation curve models to real gas and real liquid conditions. Fugacity coefficient models based on real gas equations of state, such as the Soave–Redlich–Kwong equation of state, or activity coefficient models, such as the UNIFAC model [84–86], may be coupled with adapted equilibrium distillation calculations.

Future studies may finally compare predictions based on tabulated distillation curve models with those based on distillation curve models and may develop new (general-purpose) approaches to incorporate internal heat and mass transfer based on previously underlined interpolation concepts [55].

CRediT authorship contribution statement

Maximilian Dammann: Writing – review & editing, Writing – original draft, Visualisation, Validation, Software, Methodology, Investigation, Formal analysis, Data curation, Conceptualisation. **Marco Mancini:** Writing – review & editing, Supervision. **Thomas Kolb:** Supervision, Project administration, Funding acquisition. **Roman Weber:** Writing – review & editing, Supervision.

Declaration of competing interest

The authors declare that they have no known competing financial interests or personal relationships that could have appeared to influence the work reported in this paper.

Acknowledgements

The authors thank (i) the Helmholtz Association of German Research Centres (HGF) for funding the programmes Energy Efficiency, Materials and Resources (EMR) and Materials and Technologies for the Energy Transition (MTET) and (ii) Michael Stöhr and Stephan Ruoff (German Aerospace Centre, Institute of Combustion Technology) for providing experimental data.

Supplementary material

Supplementary material related to this article can be found online at https://doi.org/10.1016/j.icheatmasstransfer.2026.111078.

Data availability

Data will be made available on request.

References

[1] C. Ledier, M. Orain, F. Grisch, J. Kashdan, G. Bruneaux, Vapour concentration measurements in biofuel sprays using innovative planar laser-induced fluorescence strategies, in: Proceedings of the 24th European Conference on Liquid Atomization and Spray Systems, 5-7 September 2011, Estoril, Portugal, ILASS Europe, 2011.

[2] S.M. Sarathy, G. Kukkadapu, M. Mehl, W. Wang, T. Javed, S. Park, M.A. Oehlschlaeger, A. Farooq, W.J. Pitz, C.-J. Sung, Ignition of alkane-rich FACE gasoline fuels and their surrogate mixtures, Proc. Combust. Inst. 35 (1) (2015) 249–257, http://dx.doi.org/10.1016/j.proci.2014.05.122.

[3] T. Edwards, Reference jet fuels for combustion testing, in: Proceedings of the 55th AIAA Aerospace Sciences Meeting, 9-13 January 2017, Grapevine, TX, USA, No. 2017-0146, American Institute of Aeronautics and Astronautics, 2017, http://dx.doi.org/10.2514/6.2017-0146.

[4] M. Stöhr, S. Ruoff, B. Rauch, W. Meier, P. Le Clercq, Droplet vaporization for conventional and alternative jet fuels at realistic temperature conditions: Systematic measurements and numerical modeling, Proc. Combust. Inst. 38 (2) (2021) 3269–3276, http://dx.doi.org/10.1016/j.proci.2020.05.015.

[5] J. Schlottke, B. Weigand, Direct numerical simulation of evaporating droplets, J. Comput. Phys. 227 (10) (2008) 5215–5237, http://dx.doi.org/10.1016/j.jcp.2008.01.042.

[6] R. Banerjee, Numerical investigation of evaporation of a single ethanol/iso-octane droplet, Fuel 107 (2013) 724–739, http://dx.doi.org/10.1016/j.fuel.2013.01.003.

[7] N. Ghata, B.D. Shaw, Computational modeling of the effects of support fibers on evaporation of fiber-supported droplets in reduced gravity, Int. J. Heat Mass Transfer 77 (2014) 22–36, http://dx.doi.org/10.1016/j.ijheatmasstransfer.2014.04.074.

[8] G. Strotos, I. Malgarinos, N. Nikolopoulos, M. Gavaises, Predicting the evaporation rate of stationary droplets with the VOF methodology for a wide range of ambient temperature conditions, Int. J. Therm. Sci. 109 (2016) 253–262, http://dx.doi.org/10.1016/j.ijthermalsci.2016.06.022.

[9] O.A. George, J. Xiao, C.S. Rodrigo, R. Mercadé-Prieto, J. Sempere, X.D. Chen, Detailed numerical analysis of evaporation of a micrometer water droplet suspended on a glass filament, Chem. Eng. Sci. 165 (2017) 33–47, http://dx.doi.org/10.1016/j.ces.2017.02.038.

[10] A.E. Saufi, A. Frassoldati, T. Faravelli, A. Cuoci, DropletSMOKE++: A comprehensive multiphase CFD framework for the evaporation of multidimensional fuel droplets, Int. J. Heat Mass Transfer 131 (2019) 836–853, http://dx.doi.org/10.1016/j.ijheatmasstransfer.2018.11.054.

[11] B. Abramzon, W.A. Sirignano, Droplet vaporization model for spray combustion calculations, Int. J. Heat Mass Transfer 32 (9) (1989) 1605–1618, http://dx.doi.org/10.1016/0017-9310(89)90043-4.

[12] M. Dammann, Numerical modelling and simulation of atmospheric entrained flow gasification of surrogate fuels (Ph.D. Thesis), Fakultät für Chemieingenieurwesen und Verfahrenstechnik, Karlsruher Institut für Technologie, Karlsruhe, Germany, 2024, http://dx.doi.org/10.5445/IR/1000172116.

[13] M. Mancini, M. Alberti, M. Dammann, U. Santo, G. Eckel, T. Kolb, R. Weber, Entrained flow gasification. Part 2: Mathematical modeling of the gasifier using RANS method, Fuel 225 (2018) 596–611, http://dx.doi.org/10.1016/j.fuel.2018.03.100.

[14] G. Eckel, Large eddy simulation of turbulent reacting multi-phase flows (Ph.D. Thesis), Fakultät für Luft- und Raumfahrttechnik und Geodäsie, Universität Stuttgart, Stuttgart, Germany, 2018, http://dx.doi.org/10.18419/opus-9941.

[15] S. Dooley, S. Hee Won, M. Chaos, J. Heyne, Y. Ju, F.L. Dryer, K. Kumar, C.-J. Sung, H. Wang, M.A. Oehlschlaeger, R.J. Santoro, T.A. Litzinger, A jet fuel surrogate formulated by real fuel properties, Combust. Flame 157 (12) (2010) 2333–2339, http://dx.doi.org/10.1016/j.combustflame.2010.07.001.

[16] L. Poulton, O. Rybdylova, I.A. Zubrilin, S.G. Matveev, N.I. Gurakov, M. Al Qubeissi, N. Al-Esawi, T. Khan, S.S. Sazhin V.M. Gun'ko, Modelling of multi-component kerosene and surrogate fuel droplet heating and evaporation characteristics: A comparative analysis, Fuel 269 (2020) 117115, http://dx.doi.org/10.1016/j.fuel.2020.117115.

[17] A. Ahmed, G. Goteng, V.S.B. Shankar, K. Al-Qurashi, W.L. Roberts, S.M. Sarathy, A computational methodology for formulating gasoline surrogate fuels with accurate physical and chemical kinetic properties, Fuel 143 (2015) 290–300, http://dx.doi.org/10.1016/j.fuel.2014.11.022.

[18] A.E. Elwardany, S.S. Sazhin, H.G. Im, A new formulation of physical surrogates of FACE A gasoline fuel based on heating and evaporation characteristics, Fuel 176 (2016) 56–62, http://dx.doi.org/10.1016/j.fuel.2016.02.041.

[19] Y. Ra, R.D. Reitz, A combustion model for multi-component fuels using a physical surrogate group chemistry representation (PSGCR), Combust. Flame 162 (10) (2015) 3456–3481, http://dx.doi.org/10.1016/j.combustflame.2015.05.014.

[20] N. Al-Esawi, M. Al Qubeissi, A new approach to formulation of complex fuel surrogates, Fuel 283 (2021) 118923, http://dx.doi.org/10.1016/j.fuel.2020.118923.

[21] A. Elwardany, J. Badra, J. Sim, M. Khurshid, M. Sarathy, H. Im, Modeling of heating and evaporation of FACE I gasoline fuel and its surrogates, in: SAE Technical Paper Series, no. 2016-01-0878, SAE International, 2016, http://dx.doi.org/10.4271/2016-01-0878.

[22] L. Zhang, S.-C. Kong, Multicomponent vaporization modeling of bio-oil and its mixtures with other fuels, Fuel 95 (2012) 471–480, http://dx.doi.org/10.1016/j.fuel.2011.12.009.

[23] A.G. Abdul Jameel, N. Naser, G. Issayev, J. Touitou, M.K. Ghosh, A.-H. Emwas, A. Farooq, S. Dooley, S.M. Sarathy, A minimalist functional group (MFG) approach for surrogate fuel formulation, Combust. Flame 192 (2018) 250–271, http://dx.doi.org/10.1016/j.combustflame.2018.01.036.

[24] A.G. Abdul Jameel, N. Naser, A.-H. Emwas, S.M. Sarathy, Surrogate formulation for diesel and jet fuels using the minimalist functional group (MFG) approach, Proc. Combust. Inst. 37 (4) (2019) 4663–4671, http://dx.doi.org/10.1016/j.proci.2018.09.035.

[25] M. Rachner, Die Stoffeigenschaften von Kerosin Jet A-1, Tech. Rep. 98–01, Deutsches Zentrum für Luft- und Raumfahrt, Köln, Germany, 1998, https://elib.dlr.de/3185/.

[26] Y. Ra, R.D. Reitz, A vaporization model for discrete multi-component fuel sprays, Int. J. Multiph. Flow 35 (2) (2009) 101–117, http://dx.doi.org/10.1016/j.ijmultiphaseflow.2008.10.006.

[27] Y. Ra, R.D. Reitz, A combustion model for IC engine combustion simulations with multi-component fuels, Combust. Flame 158 (1) (2011) 69–90, http://dx.doi.org/10.1016/j.combustflame.2010.07.019.

[28] A.E. Elwardany, S.S. Sazhin, A. Farooq, Modelling of heating and evaporation of gasoline fuel droplets: A comparative analysis of approximations, Fuel 111 (2013) 643–647, http://dx.doi.org/10.1016/j.fuel.2013.03.030.

[29] K. Mati, A. Ristori, S. Gaïl, G. Pengloan, P. Dagaut, The oxidation of a diesel fuel at 1-10 atm: Experimental study in a JSR and detailed chemical kinetic modeling, Proc. Combust. Inst. 31 (2) (2007) 2939–2946, http://dx.doi.org/10.1016/j.proci.2006.07.073.

[30] R.S.G. Baert, A mathematical model for heavy fuel droplet vaporization and pyrolysis in a high temperature inert gas, Combust. Sci. Technol. 90 (1–4) (1993) 125–147, http://dx.doi.org/10.1080/00102209308907607.

[31] V.B. Garaniya, Modelling of heavy fuel oil spray combustion using continuous thermodynamics (Ph.D. Thesis), National Centre for Maritime Engineering and Hydrodynamics, Australian Maritime College, University of Tasmania, Launceston, TAS, Australia, 2009, http://dx.doi.org/10.25959/23206451.

[32] J. Tamim, W.L.H. Hallett, A continuous thermodynamics model for multi-component droplet vaporization, Chem. Eng. Sci. 50 (18) (1995) 2933–2942, http://dx.doi.org/10.1016/0009-2509(95)00131-n.

[33] W.L.H. Hallett, A simple model for the vaporization of droplets with large numbers of components, Combust. Flame 121 (1–2) (2000) 334–344, http://dx.doi.org/10.1016/s0010-2180(99)00144-3.

[34] Z. Abdel-Qader, W.L.H. Hallett, The role of liquid mixing in evaporation of complex multicomponent mixtures: Modelling using continuous thermodynamics, Chem. Eng. Sci. 60 (6) (2005) 1629–1640, http://dx.doi.org/10.1016/j.ces.2004.10.015.

[35] W.L.H. Hallett, N.A. Clark, A model for the evaporation of biomass pyrolysis oil droplets, Fuel 85 (4) (2006) 532–544, http://dx.doi.org/10.1016/j.fuel.2005.08.006.

[36] W.L.H. Hallett, S. Beauchamp-Kiss, Evaporation of single droplets of ethanol-fuel oil mixtures, Fuel 89 (9) (2010) 2496–2504, http://dx.doi.org/10.1016/j.fuel.2010.03.007.
[37] W.L.H. Hallett, N.V. Legault, Modelling biodiesel droplet evaporation using continuous thermodynamics, Fuel 90 (3) (2011) 1221–1228, http://dx.doi.org/10.1016/j.fuel.2010.11.035.
[38] K. Harstad, P. Le Clercq, J. Bellan, A robust statistical model for the evaporation of multicomponent-fuel drops, in: Proceedings of the 41st Aerospace Sciences Meeting and Exhibit, 6-9 January 2003, Reno, NV, USA, no. 2003-1321, American Institute of Aeronautics and Astronautics, 2003, http://dx.doi.org/10.2514/6.2003-1321.
[39] K. Harstad, J. Bellan, Modeling evaporation of Jet A, JP-7, and RP-1 drops at 1 to 15 bars, Combust. Flame 137 (1–2) (2004) 163–177, http://dx.doi.org/10.1016/j.combustflame.2004.01.012.
[40] G.-S. Zhu, R.D. Reitz, A model for high-pressure vaporization of droplets of complex liquid mixtures using continuous thermodynamics, Int. J. Heat Mass Transfer 45 (3) (2002) 495–507, http://dx.doi.org/10.1016/s0017-9310(01)00173-9.
[41] S.K. Aggarwal, H.C. Mongia, Multicomponent and high-pressure effects on droplet vaporization, J. Eng. Gas Turbines Power 124 (2) (2002) 248–255, http://dx.doi.org/10.1115/1.1423640.
[42] Y. Ra, R.D. Feitz, A model for droplet vaporization for use in gasoline and HCCI engine applications, J. Eng. Gas Turbines Power 126 (2) (2004) 422–428, http://dx.doi.org/10.1115/1.1688367.
[43] S. Yang, Y. Ra, R.D. Reitz, B. VanDerWege, J. Yi, Development of a realistic multicomponent fuel evaporation model, At. Sprays 20 (11) (2010) 965–981, http://dx.doi.org/10.1615/atomizspr.v20.i11.40.
[44] E. Tolonen, W.L.H. Hallett, C.M. Monreal, Droplet evaporation behaviour of a liquid fuel from chicken litter, Fuel 139 (2015) 26–34, http://dx.doi.org/10.1016/j.fuel.2014.08.017.
[45] G. Eckel, J. Grohmann, L. Cantu, N. Slavinskaya, T. Kathrotia, M. Rachner, P. Le Clercq, W. Meier, M. Aigner, LES of a swirl-stabilized kerosene spray flame with a multi-component vaporization model and detailed chemistry, Combust. Flame 207 (2019) 134–152, http://dx.doi.org/10.1016/j.combustflame.2019.05.011.
[46] P.C. Le Clercq, J. Bellan, Direct numerical simulation of a transitional temporal mixing layer laden with multicomponent-fuel evaporating drops using continuous thermodynamics, Phys. Fluids 16 (6) (2004) 1884–1907, http://dx.doi.org/10.1063/1.1688327.
[47] P.C. Le Clercq, J. Bellan, Direct numerical simulation of gaseous mixing layers laden with multicomponent-liquid drops: Liquid-specific effects, J. Fluid Mech. 533 (2005) 57–94, http://dx.doi.org/10.1017/s0022112005003940.
[48] L. Zhang, S.-C. Kong, Vaporization modeling of petroleum–biofuel drops using a hybrid multi-component approach, Combust. Flame 157 (11) (2010) 2165–2174, http://dx.doi.org/10.1016/j.combustflame.2010.05.011.
[49] L. Zhang, S.-C. Kong, High-pressure vaporization modeling of multi-component petroleum–biofuel mixtures under engine conditions, Combust. Flame 158 (9) (2011) 1705–1717, http://dx.doi.org/10.1016/j.combustflame.2011.01.002.
[50] P. Yi, W. Long, M. Jia, L. Feng, J. Tian, Development of an improved hybrid multi-component vaporization model for realistic multi-component fuels, Int. J. Heat Mass Transfer 77 (2014) 173–184, http://dx.doi.org/10.1016/j.ijheatmasstransfer.2014.05.008.
[51] S.S. Sazhin, A.E. Elwardany, E.M. Sazhina, M.R. Heikal, A quasi-discrete model for heating and evaporation of complex multicomponent hydrocarbon fuel droplets, Int. J. Heat Mass Transfer 54 (19–20) (2011) 4325–4332, http://dx.doi.org/10.1016/j.ijheatmasstransfer.2011.05.012.
[52] S.S. Sazhin, M. Al Qubeissi, R. Nasiri, V.M. Gun'ko, A.E. Elwardany, F. Lemoine, F. Grisch, M.R. Heikal, A multi-dimensional quasi-discrete model for the analysis of diesel fuel droplet heating and evaporation, Fuel 129 (2014) 238–266, http://dx.doi.org/10.1016/j.fuel.2014.03.028.
[53] M. Al Qubeissi, S.S. Sazhin, J. Turner, S. Begg, C. Crua, M.R. Heikal, Modelling of gasoline fuel droplets heating and evaporation, Fuel 159 (2015) 373–384, http://dx.doi.org/10.1016/j.fuel.2015.06.028.
[54] A.E. Elwardany, S.S. Sazhin, A quasi-discrete model for droplet heating and evaporation: Application to diesel and gasoline fuels, Fuel 97 (2012) 685–694, http://dx.doi.org/10.1016/j.fuel.2012.01.068.
[55] J.S. Chin, An engineering calculation method for multi-component stagnant droplet evaporation with finite diffusivity, in: Proceedings of the ASME 1994 International Gas Turbine and Aeroengine Congress and Exposition. Volume 3: Coal, Biomass and Alternative Fuels; Combustion and Fuels; Oil and Gas Applications; Cycle Innovations, 13–16 June 1994, The Hague, The Netherlands, American Society of Mechanical Engineers, 1994, http://dx.doi.org/10.1115/94-gt-440.
[56] K. Prommersberger, G. Maier, S. Wittig, Validation and application of a droplet evaporation model for real aviation fuel, in: Proceedings of the RTO Applied Vehicle Technology Panel (AVT) Symposium on Gas Turbine Engine Combustion Emissions and Alternative Fuels, 12-16 October, Lisbon, Portugal, 1998, pp. 16–1–16–13.
[57] K. Prommersberger, Untersuchung der Gemischaufbereitung in Gasturbinenbrennkammern unter Berücksichtigung der Eigenschaften kommerzieller Flüssigbrennstoffe (Ph.D. Thesis), Fakultät für Maschinenbau, Universität Karlsruhe, Karlsruhe, Germany, 2004.
[58] M. Burger, R. Schmehl, K. Prommersberger, O. Schäfer, R. Koch, S. Wittig, A multi-component droplet evaporation model for real aviation fuels at elevated pressures, in: Proceedings of the 18th European Conference on Liquid Atomization and Spray Systems, 9-11 September 2002, Saragossa, Spain, ILASS Europe, 2002, http://www.ilasseurope.org/ICLASS/ilass2002/papers/050.pdf.
[59] M. Burger, R. Schmehl, K. Prommersberger, O. Schäfer, R. Koch, S. Wittig, Droplet evaporation modeling by the distillation curve model: Accounting for kerosene fuel and elevated pressures, Int. J. Heat Mass Transfer 46 (23) (2003) 4403–4412, http://dx.doi.org/10.1016/s0017-9310(03)00286-2.
[60] A. Makino, C.K. Law, On the controlling parameter in the gasification behavior of multicomponent droplets, Combust. Flame 73 (3) (1988) 331–336, http://dx.doi.org/10.1016/0010-2180(88)90027-2.
[61] M.F. Bardon, V.K. Rao, Calculation of gasoline volatility, J. Inst. Fuel 57 (432) (1984) 342–349.
[62] M.F. Bardon, V.K. Rao, R. Vaivads, M.J.B. Evans, Measured and predicted effect of the extent of evaporation on gasoline vapour pressure, J. Inst. Fuel 59 (432) (1986) 216–221.
[63] J.E.D. Gauthier, M.F. Bardon, V.K. Rao, Combustion characteristics of multicomponent fuels under cold starting conditions in a gas turbine, in: Proceedings of the ASME 1991 International Gas Turbine and Aeroengine Congress and Exposition. Volume 3: Coal, Biomass and Alternative Fuels; Combustion and Fuels; Oil and Gas Applications; Cycle Innovations, 3-6 June 1991, Orlando, FL, USA, American Society of Mechanical Engineers, 1991, http://dx.doi.org/10.1115/91-gt-109.
[64] M. Burger, Gemischbildung in Hochdruckbrennkammern: numerische Ansätze zur Berechnung instationärer Zweiphasenströmungen (Ph.D. Thesis), Fakultät für Maschinenbau, Universität Karlsruhe, Karlsruhe, Germany, 2005.
[65] H.G. Rackett, Equation of state for saturated liquids, Journal of Chemical & Engineering Data 15 (4) (1970) 514–517, http://dx.doi.org/10.1021/je60047a012.
[66] P.B. Govindaraju, M. Ihme, Group contribution method for multicomponent evaporation with application to transportation fuels, Int. J. Heat Mass Transfer 102 (2016) 833–845, http://dx.doi.org/10.1016/j.ijheatmasstransfer.2016.06.079.
[67] S.C. Burke, M. Ratcliff, R. McCormick, R. Rhoads, B. Windom, Distillation-based droplet modeling of non-ideal oxygenated gasoline blends: Investigating the role of droplet evaporation on PM emissions, SAE International Journal of Fuels and Lubricants 10 (1) (2017) 69–81, http://dx.doi.org/10.4271/2017-01-0581.
[68] J.L. Burger, T.J. Bruno, Application of the advanced distillation curve method to the variability of jet fuels, Energy & Fuels 26 (6) (2012) 3661–3671, http://dx.doi.org/10.1021/ef3006178.
[69] E. Weber de Menezes, R. da Silva, R. Cataluña, R.J.C. Ortega, Effect of ethers and ether/ethanol additives on the physicochemical properties of diesel fuel and on engine tests, Fuel 85 (5–6) (2006) 815–822, http://dx.doi.org/10.1016/j.fuel.2005.08.027.
[70] ASTM International, D86-20a. Standard test method for distillation of petroleum products and liquid fuels at atmospheric pressure, 2020, http://dx.doi.org/10.1520/D0086-20A.
[71] T.J. Bruno, Improvements in the measurement of distillation curves. 1. A composition-explicit approach, Industrial & Engineering Chemistry Research 45 (12) (2006) 4371–4380, http://dx.doi.org/10.1021/ie051393j.
[72] A.M. Ferris, D.A. Rothamer, Methodology for the experimental measurement of vapor–liquid equilibrium distillation curves using a modified ASTM D86 setup, Fuel 182 (2016) 467–479, http://dx.doi.org/10.1016/j.fuel.2016.05.099.
[73] ASTM International, D7896-19. Standard test method for thermal conductivity, thermal diffusivity, and volumetric heat capacity of engine coolants and related fluids by transient hot wire liquid thermal conductivity method, 2019, http://dx.doi.org/10.1520/D7896-19.
[74] M.E. Harries, A.G. McDonald, T.J. Bruno, Measuring the distillation curves of non-homogeneous fluids: Method and case study of two pyrolysis oils, Fuel 204 (2017) 23–27, http://dx.doi.org/10.1016/j.fuel.2017.04.066.
[75] Aspen Technology, Aspen Properties. Release V10, 2017, https://www.aspentech.com/products/aspen-properties.aspx.
[76] L. Constantinou, R. Gani, New group contribution method for estimating properties of pure compounds, AIChE Journal 40 (10) (1994) 1697–1710, http://dx.doi.org/10.1002/aic.690401011.
[77] B.I. Lee, M.G. Kesler, A generalized thermodynamic correlation based on three-parameter corresponding states, AIChE Journal 21 (3) (1975) 510–527, http://dx.doi.org/10.1002/aic.690210313.
[78] B.E. Poling, J.M. Prausnitz, J.P. O'Connell, The properties of gases and liquids, fifth ed., McGraw-Hill, New York, NY, USA, 2001.
[79] A. Bondi, Physical properties of molecular crystals, liquids, and glasses, first ed., John Wiley & Sons, New York, NY, USA [et al.], 1968.
[80] Y. Nannoolal, J. Rarey, D. Ramjugernath, W. Cordes, Estimation of pure component properties. Part 1: Estimation of the normal boiling point of non-electrolyte organic compounds via group contributions and group interactions, Fluid Phase Equilib. 226 (2004) 45–63, http://dx.doi.org/10.1016/j.fluid.2004.09.001.

[81] Y. Nannoolal, J. Rarey, D. Ramjugernath, Estimation of pure component properties. Part 2: Estimation of critical property data by group contribution, Fluid Phase Equilibria 252 (1-2) (2007) 1–27, http://dx.doi.org/10.1016/j.fluid.2006.11.014.

[82] Y. Nannoolal, J. Rarey, D. Ramjugernath, Estimation of pure component properties. Part 3: Estimation of the vapor pressure of non-electrolyte organic compounds via group contributions and group interactions, Fluid Phase Equilib. 269 (1–2) (2008) 117–133, http://dx.doi.org/10.1016/j.fluid.2008.04.020.

[83] B. Moller, J. Rarey, D. Ramjugernath, Estimation of the vapour pressure of non-electrolyte organic compounds via group contributions and group interactions, J. Mol. Liq. 143 (1) (2008) 52–63, http://dx.doi.org/10.1016/j.molliq.2008.04.020.

[84] A. Fredenslund, R.L. Jones, J.M. Prausnitz, Group-contribution estimation of activity coefficients in nonideal liquid mixtures, AIChE Journal 21 (6) (1975) 1086–1099, http://dx.doi.org/10.1002/aic.690210607.

[85] A. Fredenslund, Vapor–liquid equilibria using UNIFAC: A group contribution method, first ed., Elsevier Scientific Publishers, Amsterdam, The Netherlands [et al.], 1977.

[86] A. Fredenslund, J. Gmehling, M.L. Michelsen, P. Rasmussen, J.M. Prausnitz, Computerized design of multicomponent distillation columns using the UNIFAC group contribution method for calculation of activity coefficients, Industrial & Engineering Chemistry Process Design and Development 16 (4) (1977) 450–462, http://dx.doi.org/10.1021/i260064a004.

[87] B.J. McBride, M.J. Zehe, S. Gordon, NASA Glenn coefficients for calculating thermodynamic properties of individual species, Tech. Rep. NASA/TP-2002-211556, John H. Glenn Research Center at Lewis Field, National Aeronautics and Space Administration, Cleveland, OH, USA, 2002, https://ntrs.nasa.gov/citations/20020085330.

[88] L.S. Tee, S. Gotoh, W.E. Stewart, Molecular parameters for normal fluids, Lennard-Jones 12–6 potential, Industrial & Engineering Chemistry Fundamentals 5 (3) (1966) 356–363, http://dx.doi.org/10.1021/i160019a011.

[89] L.R. Perkins, C.J. Geankoplis, Molecular diffusion in a ternary liquid system with the diffusing component dilute, Chem. Eng. Sci. 24 (7) (1969) 1035–1042, http://dx.doi.org/10.1016/0009-2509(69)80075-8.

[90] C.R. Wilke, A viscosity equation for gas mixtures, J. Chem. Phys. 18 (4) (1950) 517–519, http://dx.doi.org/10.1063/1.1747673.

[91] L. Grunberg, A.H. Nissan, Mixture law for viscosity, Nature 164 (4175) (1949) 799–800, http://dx.doi.org/10.1038/164799b0.

[92] ANSYS, ANSYS Fluent theory guide. Release 2020 R2, Canonsburg, PA, USA, 2020.

[93] S.A. Morsi, A.J. Alexander, An investigation of particle trajectories in two-phase flow systems, J. Fluid Mech. 55 (2) (1972) 193–208, http://dx.doi.org/10.1017/s0022112072001806.

[94] S. Tonini, G.E. Cossali, A novel formulation of multi-component drop evaporation models for spray applications, Int. J. Therm. Sci. 89 (2015) 245–253, http://dx.doi.org/10.1016/j.ijthermalsci.2014.10.016.

[95] S. Tonini, G.E. Cossali, A novel vaporisation model for a single-component drop in high temperature air streams, Int. J. Therm. Sci. 75 (2014) 194–203, http://dx.doi.org/10.1016/j.ijthermalsci.2013.08.004.

[96] M.C. Yuen, L.W. Chen, On drag of evaporating liquid droplets, Combust. Sci. Technol. 14 (4–6) (1976) 147–154, http://dx.doi.org/10.1080/00102207608547524.

[97] W.E. Ranz, W.R. Marshall, Evaporation from drops. Part I, Chem. Eng. Prog. 48 (3) (1952) 141–146.

[98] W.E. Ranz, W.R. Marshall, Evaporation from drops. Part II, Chem. Eng. Prog. 48 (3) (1952) 173–180.

[99] M. Stöhr, S. Ruoff, B. Rauch, W. Meier, P. Le Clercq, Experimental study of droplet vaporization for conventional and renewable transportation fuels: Effects of physical properties and chemical composition, Fuel 356 (2024) 129535, http://dx.doi.org/10.1016/j.fuel.2023.129535.

[100] S. Dooley, M. Uddi, S.H. Won, F.L. Dryer, Y. Ju, Methyl butanoate inhibition of *n*-heptane diffusion flames through an evaluation of transport and chemical kinetics, Combust. Flame 159 (4) (2012) 1371–1384, http://dx.doi.org/10.1016/j.combustflame.2011.09.016.